



**HAL**  
open science

## Modelling the behaviour of bentonite pellet-powder mixtures upon hydration from dry granular state to saturated homogeneous state

Benjamin Darde, Patrick Dangla, Jean-Noël Roux, Jean-Michel Pereira, Jean Talandier, Minh Ngoc Vu, Anh Minh A.M. Tang

### ► To cite this version:

Benjamin Darde, Patrick Dangla, Jean-Noël Roux, Jean-Michel Pereira, Jean Talandier, et al.. Modelling the behaviour of bentonite pellet-powder mixtures upon hydration from dry granular state to saturated homogeneous state. *Engineering Geology*, 2020, 278, pp.105847. 10.1016/j.enggeo.2020.105847 . hal-03053646

**HAL Id: hal-03053646**

**<https://enpc.hal.science/hal-03053646>**

Submitted on 11 Dec 2020

**HAL** is a multi-disciplinary open access archive for the deposit and dissemination of scientific research documents, whether they are published or not. The documents may come from teaching and research institutions in France or abroad, or from public or private research centers.

L'archive ouverte pluridisciplinaire **HAL**, est destinée au dépôt et à la diffusion de documents scientifiques de niveau recherche, publiés ou non, émanant des établissements d'enseignement et de recherche français ou étrangers, des laboratoires publics ou privés.

**Title:**

Modelling the behaviour of bentonite pellet-powder mixtures upon hydration from dry granular state to saturated homogeneous state

**Authors:**

Benjamin Darde<sup>1,2</sup>: benjamin.darde@enpc.fr

Patrick Dangla<sup>1</sup>: patrick.dangla@univ-eiffel.fr

Jean-Noël Roux<sup>1</sup>: jean-noel.roux@univ-eiffel.fr

Jean-Michel Pereira<sup>1</sup>: jean-michel.pereira@enpc.fr

Jean Talandier<sup>2</sup>: jean.talandier@andra.fr

Minh Ngoc Vu<sup>2</sup>: minh-ngoc.vu@andra.fr

Anh Minh Tang<sup>1</sup>: anh-minh.tang@enpc.fr

**Affiliations:**

<sup>1</sup>: Navier, Ecole des Ponts, Univ Gustave Eiffel, CNRS, Marne-la-Vallée, France

<sup>2</sup>: French national radioactive waste management agency (Andra), France

**Corresponding author:**

Anh Minh Tang

Ecole des Ponts ParisTech

6-8 avenue Blaise Pascal

Cité Descartes – Champs-sur-Marne

77455 Marne-la-Vallée cedex 2

anh-minh.tang@enpc.fr

**Abstract:**

Bentonite pellet-powder mixtures are candidate materials for sealing the galleries in deep geological repositories for radioactive waste. In the present work, swelling pressure tests are performed on pellet-powder mixtures with different powder contents. Results highlight the influence of the initial granular structure on the mechanical behaviour of pellet-powder mixtures. In mixtures with a low density powder in the inter-pellet porosity, the macroscopic response of pellet-powder mixtures is identical to that of a pellet assembly with no powder. A model is proposed to describe the hydromechanical behaviour of pellet-powder mixtures. The formulation considers two distinct states of the material, Granular and Continuous. In the Granular state, the pellets control the mechanical behaviour of the mixture. In the Continuous state, both pellets and powder contribute to the mechanical behaviour of the mixture. In the Granular domain, the material behaviour is described by constitutive laws proposed after a numerical study using Discrete Element Method. In the Continuous domain, the material behaviour is described by a modified Barcelona Basic Model. Transition between the two domains depends on the density of the powder phase and suction. The model is implemented in a Finite Element Method code, and the swelling pressure tests performed in the laboratory are simulated with a single set of parameters. These results improve the knowledge on the behaviour of bentonite pellet-powder mixtures during hydration in repository conditions.

**Keywords:**

Expansive soil, Pellets, Swelling pressure, Discrete Element Method, Finite Element Method, Constitutive modelling

### List of notations:

$(e)$	Elastic (superscript)
$(p)$	Plastic (superscript)
$\dot{\epsilon}$	Strain rate of the periodic cell in DEM
$a$	Sphere diameter in DEM
$a_0$	Initial sphere diameter in DEM
$C_A$	Model parameter
$dX$	Increment of $X$
$D$	Pellet diameter
$D_{cell}$	Diameter of the isochoric cell
$D_{sensor}$	Diameter of the sensor
$e$	Total void ratio
$e_0$	Initial value of $e$
$E_I$	Pellet Young modulus
$e_1$	Pellet void ratio
$e_{10}$	Initial value of $e_1$
$e_2$	Powder grains void ratio
$e_{20}$	Initial value of $e_2$
$e_M$	Macrostructural void ratio
$e_m$	Microstructural void ratio
$e_{m0}$	Initial value of $e_m$
$e_{M0}$	Initial value of $e_M$
$f_{m a}$	Model parameter related to contact plasticity
$f_{m b}$	Model parameter related to contact plasticity
$f_{Mm}$	Model parameter
$F_N$	Normal contact force

$F_{N0}$	Initial value of $F_N$
$F_{N\alpha}$	$\alpha$ -coordinates of the contact force $F_N$
$F_N^*$	Mean contact normal force in the granular assembly
$F_T$	Tangential reaction vector
$f_\varepsilon$	Dimensionless stiffness parameter for the granular assembly
$f_{\varepsilon a}$	Value of $f_\varepsilon$ if contacts are considered elastic
$f_{\varepsilon p}$	Value of $f_\varepsilon$ if contacts are considered plastic
$h$	Height of the cylinder part of the pellet
$H$	Height of the pellet
$H_{cell}$	Height of the isochoric cell
$I$	Dimensionless inertia parameter
$k_s$	Model parameter
$M$	Slope of the critical state line
$m_l$	Mass of the pellet
$m_g$	Dimensionless pressure parameter
$m_g^*$	Limit value of $m_g$
$N_l$	Number of spheres in DEM
$N_c$	Number of contacts
$n_p$	Model parameter related to the initial elastic limit
$p$	Total mean stress
$p^*$	Elastic limit
$p'$	Effective mean stress
$p'_0$	Initial effective mean stress
$p'_1$	Effective mean stress in pellets
$p'_2$	Effective mean stress in powder grains
$p_0$	Initial value of $p$
$p_{atm}$	Atmospheric pressure

$p_c$	BBM reference stress
$p_r$	Reference stress
$q$	Deviatoric stress
$\mathbf{r}$	Vector joining the centre of particles in contact in DEM
$r$	Norm of the $\mathbf{r}$ vector
$r_0$	Initial value $r$
$R_I$	Pellet strength
$R_c$	Curvature radius of the pellet
$r_{vf}$	Ratio of volume fraction
$r_{vf}^*$	Threshold value of $r_{vf}$
$r_\alpha$	$\alpha$ -coordinates of vector $\mathbf{r}$
$s$	Total suction
$s^*$	Threshold suction
$s_0$	Initial suction
$s_1$	Suction in pellets
$s_2$	Suction in powder
$s_M$	Suction in macropores
$\mathbf{u}$	Displacement field
$x_{plas}$	Proportion of plastic contacts
$x_s$	Proportion of powder
$Z$	Coordination number
$\alpha_m$	Model parameter related to microstructural stiffness
$\beta_m$	Model parameter related to microstructural stiffness
$\delta_N$	Normal deflection
$\delta_N^*$	Average normal deflection
$\varepsilon_V$	Total volumetric strain
$\varepsilon_{V I}$	Volumetric strain of the pellet

$\varepsilon_{V2}$	Volumetric strains of the powder grains
$\varepsilon_{VM}$	Volumetric strain of the macrostructure
$\kappa$	Dimensionless elastic stiffness parameter of the macrostructure related to changes in mean stress
$\kappa_m$	Dimensionless elastic stiffness parameter of the microstructure
$\kappa_s$	Dimensionless elastic stiffness parameter of the macrostructure related to changes in suction
$\lambda$	Dimensionless elastoplastic stiffness parameter of the macrostructure
$\lambda_0$	Value of $\lambda$ in fully saturated conditions
$\nu_1$	Poisson ratio of the pellet
$\rho$	Ratio $\lambda(s \rightarrow \infty)/\lambda_0$
$\rho_d$	Dry density of the mixture
$\rho_{d10}$	Initial pellet dry density
$\rho_s$	Density of solid particles
$\sigma_{aa}$	Diagonal components of the Cauchy stress tensor
$\sigma_{xx0}$	Initial xx components of the Cauchy stress tensor
$\sigma_{yy0}$	Initial yy components of the Cauchy stress tensor
$\sigma_{zz0}$	Initial zz components of the Cauchy stress tensor
$\Phi_1$	Pellet volume fraction in experiments
$\phi_1$	Pellet volume fraction in the model
$\Phi_{10}$	Initial pellet volume fraction in experiments
$\phi_{10}$	Initial pellet volume fraction in the model
$\Phi_2$	Powder volume fraction in experiments
$\phi_2$	Powder volume fraction in the model
$\Phi_{20}$	Initial powder volume fraction in experiment
$\phi_M$	Volume fraction of macrostructural voids
$\phi_{mat}$	Volume fraction of the powder in inter-pellet voids

$\phi_{mat\ 0}$	Initial volume fraction of the powder in inter-pellet voids
$\omega$	Model parameter related to the increase in $\lambda$ with suction
$\Omega$	Total volume of the granular assembly
$\Omega_0$	Initial value of $\Omega$
$\Omega_1$	Volume of pellet
$\Omega_s$	Total volume of solid in the mixture
$\Omega_{s\ 1}$	Volume of solid in the pellets
$\Omega_{s\ 2}$	Volume of solid in the powder grains
$\Omega_v$	Total volume of voids in the mixture
$\Omega_{v\ 1}$	Volume of void in the pellets
$\Omega_{v\ 2}$	Volume of void in the powder grains
$\Omega_{v\ M}$	Volume of void between pellets and powder grains

**Funding:**

This work was funded by École des Ponts ParisTech and the French National Agency for Radioactive Waste Management (Andra).

## 1    **1.    Introduction**

2        Bentonite materials are considered as sealing materials in concepts of deep geological disposal for  
3    radioactive waste. These materials are characterised by a low permeability, good radionuclide  
4    retention capacity and ability to swell upon hydration. The latter feature allows these materials to fill  
5    technological voids and to exert a swelling pressure against the host rock, which confines the  
6    excavation damaged zone and thus reduces the fluid flow along the gallery via this zone.

7        Owing to operational convenience, pellet-based materials have been considered as an alternative to  
8    compacted blocks (Bernachy-barbe et al., 2020; Darde et al., 2018; Molinero-Guerra et al., 2017;  
9    Navarro et al., 2020a, 2020b; Sánchez et al., 2016). The material is installed in the galleries in a dry  
10   state as a granular assembly. Upon hydration by the pore water of the host rock, the granular material  
11   progressively becomes homogeneous. Before homogenisation, the mechanical behaviour of the  
12   material is controlled by its granular nature. In fully saturated conditions, the material has totally lost  
13   its initial granular structure. Its structure in these conditions is similar to fully saturated compacted  
14   blocks (Hoffmann et al., 2007; Imbert and Villar, 2006; van Geet et al., 2005). The behaviour of  
15   pellet-based materials is thus controlled by different mechanisms depending on the hydration state.

16        In mixtures of pellet and crushed pellets (powder), powder fills inter-pellet voids, increasing the  
17   total dry density of the sealing material thus its final swelling pressure (Imbert and Villar, 2006;  
18   Kaufhold et al., 2015; Lloret et al., 2003; Wang et al., 2012). Considering these mixtures as sealing  
19   materials involves challenges. For instance, powder in the inter-pellet porosity may migrate during  
20   installation and induce local heterogeneities of density. In addition, depending on the density of the  
21   powder phase, this latter can be considered to either participate in the macroscopic mechanical  
22   response, or to leave the mechanical behaviour controlled by the pellet assembly.

23        Existing modelling frameworks do not account for these particular features of pellet-powder  
24   mixtures. It is proposed in the present study to: *(i)* provide experimental evidence of the influence of  
25   the granular structure on the macroscopic response of the mixture upon hydration; *(ii)* use Discrete  
26   Element Method (DEM) to study the intrinsic behaviour of pellet assemblies; *(iii)* propose a

27 conceptual model, based on DEM results and modified existing modelling frameworks, able to  
28 satisfactorily reproduce the main features of pellet-powder mixtures upon hydration.

29 In this respect, the present study is organised as follows. First, swelling pressure tests are carried  
30 out in the laboratory on three pellet-powder mixtures, with identical pellet volume fraction and various  
31 powder volume fractions, to highlight the influence of the granular structure on the material behaviour.  
32 Experimental results are discussed and a conceptual interpretation of the behaviour of pellet mixtures  
33 is proposed. Then, DEM simulations are performed to model large pellet assemblies and determine  
34 constitutive laws. An elasto-plastic model, based on DEM results and a modified formulation of the  
35 Barcelona Basic Model (BBM) (Alonso et al., 1990) is then proposed to describe the hydromechanical  
36 behaviour of pellet-powder mixtures in granular and continuous states. The swelling pressure tests are  
37 finally simulated using the proposed model.

38

## 39 2. Swelling pressure tests

40

### 41 2.1. Tested materials

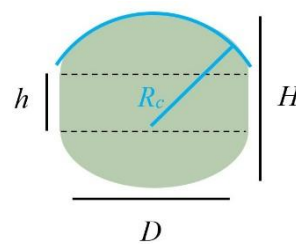
42 Pellets are made of MX80 bentonite. Pellets are composed of a cylinder-shaped part with two  
43 spherical caps at both ends (Figure 1). Pellet geometrical properties and physical properties are  
44 presented in Table 1.

45

a)

b)

46



47

48

Figure 1: a) Picture of a pellet; b) Schematic view of a pellet.

Table 1: Initial properties of the pellets.

Pellet properties	Value
<i>Geometrical properties</i>	
Diameter, $D$	7 mm
Height of the cylinder part, $h$	5 mm
Height, $H$	7 mm
Curvature radius, $R_c$	6.5 mm
<i>Physical properties</i>	
Density of solid particles, $\rho_s$ (Saba et al., 2014)	2.77 Mg/m <sup>3</sup>
Initial dry density, $\rho_{d10}$	1.91 Mg/m <sup>3</sup>
Initial void ratio, $e_{10}$	0.45
Initial suction, $s_0$	89 MPa

49 The material referred to as “powder” is obtained by crushing pellets. Initial suction of the powder is  
50 180 MPa. The average grain diameter of the powder is 0.65 mm (Molinero-Guerra et al., 2017).

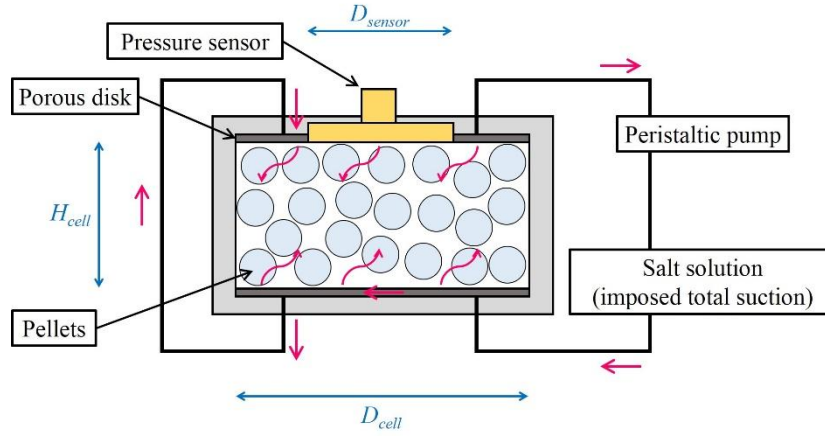
51 Three pellet-powder mixtures are prepared at the same pellet volume fraction and three different  
52 powder volume fractions. Pellet initial volume fraction,  $\Phi_{10}$  (volume of pellets / total volume), is  
53 0.553 in all samples. The three powder initial volume fractions,  $\Phi_{20}$ , are 0.236, 0.118, and 0. The  
54 highest value of  $\Phi_{20}$  corresponds to pellet/powder proportions of 70/30 in dry mass. To highlight that  
55  $\Phi_{10}$  remains identical in all samples, the three mixtures are referred to as 70/30, 70/15, and 70/0 in the  
56 following. The dry densities ( $\rho_d$ ) of the 70/30, 70/15, and 70/0 materials are 1.50 Mg/m<sup>3</sup>, 1.275 Mg/m<sup>3</sup>,  
57 and 1.05 Mg/m<sup>3</sup>, respectively.

58

## 59 2.2. Method

60 Four suction-controlled swelling pressure tests are carried out in isochoric cells. Cylindrical  
61 isochoric cells made of stainless steel are used to perform the tests (see Figure 2). Swelling pressure is

62 determined as the vertical pressure measured by a sensor on the top wall of the cell. Two porous disks  
 63 are placed at the top and bottom of the cell. The cell dimensions are: height,  $H_{cell} = 30$  mm and  
 64 diameter,  $D_{cell} = 60$  mm. The sensor diameter is  $D_{sensor} = 30$  mm.



65

66 Figure 2: Schematic view of the experimental setup. Red arrows represent humid air circulation.

67 Samples are prepared by placing pellets one by one in the isochoric cells to form a layer. Then, the  
 68 proportion of powder associated to the laid proportion of pellets is poured in the inter-pellet voids.  
 69 This procedure is followed to reduce heterogeneity of the samples (Molinero-Guerra et al., 2017).  
 70 Four samples are prepared (Table 2).

71

Table 2: Properties of the pellet-powder mixtures.

Sample	Mixture	$\Phi_{10}$	$\Phi_{20}$	$\rho_d$ : Mg/m <sup>3</sup>
SP30	70/30		0.236	1.50
SP15	70/15	0.553	0.118	1.275
SP0a	70/0		0	1.05
SP0b	70/0		0	1.05

72

73 Hydration is performed step by step using the vapour equilibrium technique (Hoffmann et al.,  
 74 2007; Lloret et al., 2003; Tang and Cui, 2005; Zhang et al., 2020) from  $s_0$  to a suction  $s = 4$  MPa. A  
 75 peristaltic pump makes air circulate through the saturated salt solution to maintain a constant target  
 76 relative humidity, then through the isochoric cell (Figure 2). Humid air is allowed to circulate directly

77 from the bottom to the top of the cell through a side tube. Thus, no excessive air pressure is developed  
78 when using the peristaltic pump and humid air is considered to diffuse freely inside the inter-pellet  
79 porosity. When the pressure measured by the sensor reaches a plateau, the subsequent suction step is  
80 imposed. Following the suction step at  $s = 4$  MPa, the sample is wetted using synthetic water of  
81 similar chemical composition as the pore water of the host rock of Meuse/Haute-Marne Underground  
82 Research Laboratory (France). Room temperature is controlled and remains constant ( $20^{\circ}\text{C} \pm 1^{\circ}\text{C}$ ).  
83 Hydration paths are summarised in Table 3. It is worth noting that hydration paths described as zero  
84 suction are performed using synthetic water, which may have an osmotic suction higher than zero as  
85 suggested by (Ferrari et al., 2014).

86 Table 3: Hydration paths followed by the samples. Suctions are given in MPa.

Sample	I	II	III	IV	V	VI	VII	VIII
SP0a	82	59	40	38	25	13	9	-
SP0b	82	59	40	25	9	4	0*	-
SP15	82	59	40	25	9	4	0*	-
SP30	82	59	40	25	13	9	4	0*

87 \*: samples wetted using synthetic liquid water

88

## 89 2.3. Experimental results and discussion

90

### 91 2.3.1. Evolution of swelling pressure upon hydration

92 Figure 3 presents the evolution of swelling pressure as a function of elapsed time for all hydration  
93 steps of the four swelling pressure tests (Table 3).

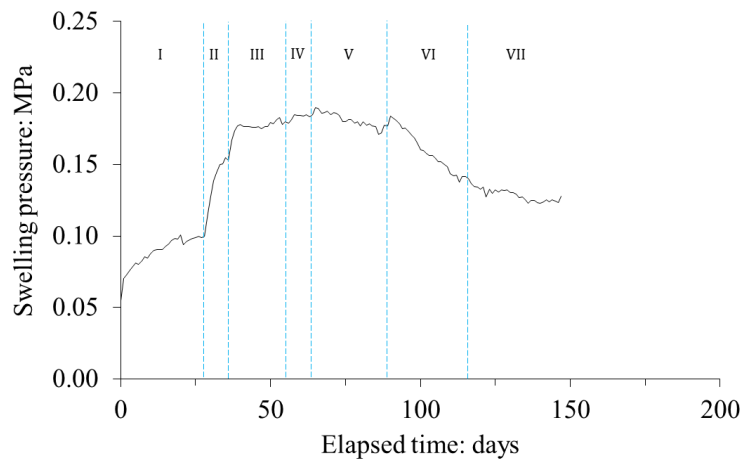
94 The swelling pressure in SP0a increases from 0.055 MPa (pressure following the closure of the  
95 cell) to 0.173 MPa, from initial state to  $s = 38$  MPa. Upon hydration from  $s = 38$  MPa to  $s = 9$  MPa,  
96 the swelling pressure decreases to 0.128 MPa.

97 The swelling pressure in SP0b increases from 0.010 MPa to 0.153 MPa, from initial state to  
98  $s = 9$  MPa. Upon hydration from  $s = 9$  MPa to  $s = 4$  MPa, the swelling pressure decreases to 0.135  
99 MPa. Following liquid water flooding, the swelling pressure increases, reaches a peak at 0.250 MPa,  
100 then stabilises at 0.247 MPa after 607 days.

101 The swelling pressure in SP15 increases from 0.015 MPa to 0.290 MPa from initial state to  $s = 40$   
102 MPa. Upon hydration from  $s = 40$  MPa to  $s = 4$  MPa, the swelling pressure decreases to 0.200 MPa.  
103 Following liquid water flooding, the swelling pressure increases and stabilises at 0.910 MPa after 622  
104 days.

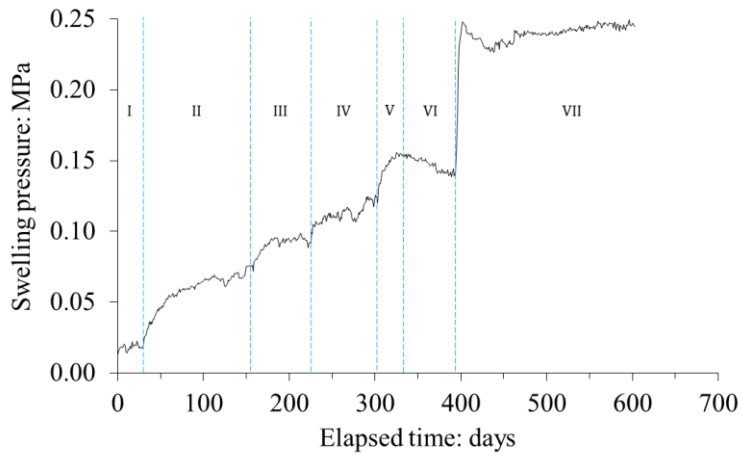
105 The swelling pressure in SP30 increases from 0.004 MPa to 1.22 MPa, from initial state to  
106  $s = 9$  MPa. Upon hydration from  $s = 9$  MPa to  $s = 4$  MPa, the swelling pressure decreases to  
107 0.650 MPa, followed by an increase to 1.36 MPa. Following liquid water flooding, the swelling  
108 pressure increases and stabilises at 4.45 MPa after 755 days.

109 a)



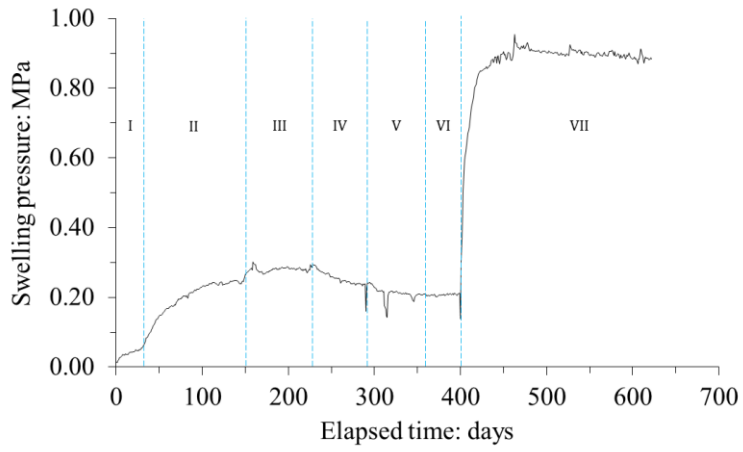
110

111 b)



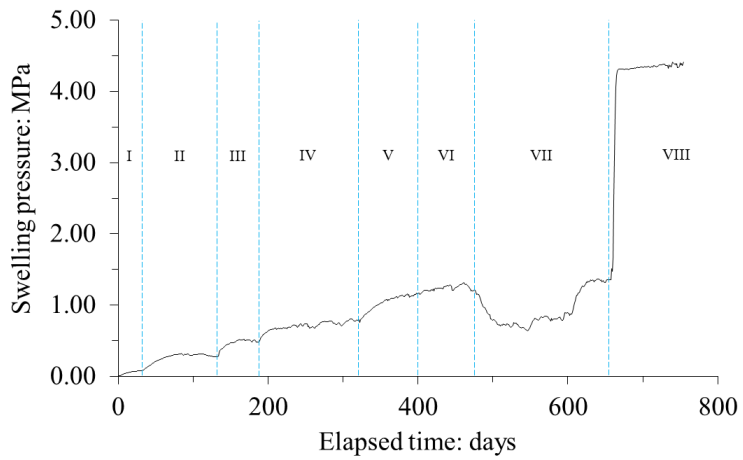
112

113 c)



114

115 d)



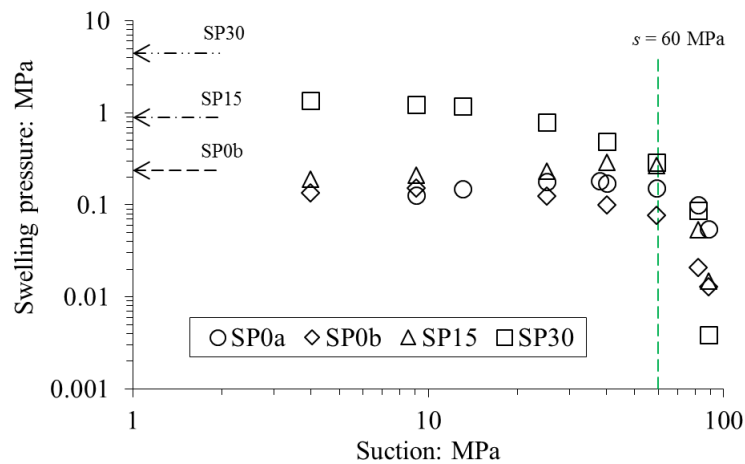
116

117 Figure 3: Evolution of swelling pressure as a function of elapsed time. a) SP0a test, b) SP0b test, c) SP15 test, d) SP30

118 test.

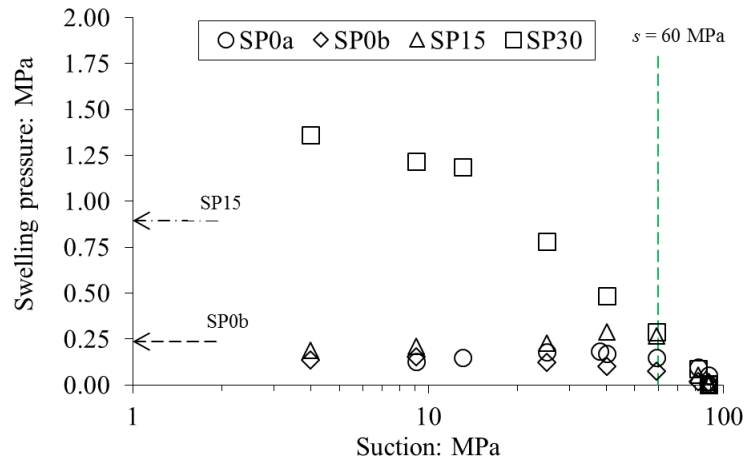
119 In Figure 4 the swelling pressure at the end of each step is plotted versus the imposed suction  
 120 corresponding to the step. Because of the wide range of swelling pressure measured upon hydration,  
 121 results of all tests are shown using a logarithmic scale in Figure 4a while a linear scale is used in  
 122 Figure 4b, but limited to swelling pressures lower than 2 MPa. It is highlighted that during the first  
 123 two hydration steps, the swelling pressure developed in 70/0 (SP0a and SP0b tests), 70/15 (SP15 test),  
 124 and 70/30 (SP30 test) materials remains within the same order of magnitude. For  $4 \text{ MPa} < s < 60 \text{ MPa}$ ,  
 125 the swelling pressure developed in the 70/30 material is significantly higher than in the 70/15 and 70/0  
 126 materials while those developed in 70/15 and 70/0 materials are still very close. Following water  
 127 flooding, the final value of swelling pressure is higher for a higher dry density of the mixture, as  
 128 previously observed in the literature (Bian et al., 2019; Imbert and Villar, 2006; Jia et al., 2019;  
 129 Kaufhold et al., 2015; Lloret et al., 2003; Wang et al., 2013, 2012).

130 a)



131

132 b)



133

134 Figure 4: Evolution of swelling pressure as a function of suction upon hydration. a) Swelling pressure on a logarithmic  
 135 scale, b) Swelling pressure on a linear scale, limited to swelling pressures lower than 2 MPa. Horizontal arrows represent the  
 136 final swelling pressure of the tested materials.

137

### 138 2.3.2. Influence of the granular structure and the powder volume fraction

139 In SP0a and SP0b tests, no powder is filling the inter-pellet voids and the material behaviour is  
 140 controlled by the granular assembly of pellets as long as the material is granular. In the course of  
 141 hydration, pellet swelling in constant-volume conditions of the sample induces an increase of inter-  
 142 granular forces and swelling pressure. As inter-granular forces reach pellet strength, swelling pressure  
 143 no longer increases and a plateau/decrease of swelling pressure is observed as suction decreases. The  
 144 influence of initial granular structure can be divided in two phases: (i) increase of inter-granular  
 145 forces, controlled by pellet stiffness; (ii) plateau/decrease of swelling pressure controlled by pellet  
 146 strength and stiffness decreasing upon wetting (Alonso et al., 2010; Darde et al., 2020b; Hoffmann et  
 147 al., 2007).

148 Comparison of the suction-swelling pressure relationships of the three materials upon hydration  
 149 suggests that the powder has a variable influence on the macroscopic response of the material. All  
 150 samples have the same pellet solid fraction but different powder contents. Differences between results  
 151 of the different tests is thus attributed to the presence of powder in the inter-pellet porosity.

152 For  $s > 60$  MPa, the influence of powder is not significant. Then, for  $4 \text{ MPa} < s < 60 \text{ MPa}$ , the  
153 response of the 70/30 material, characterised by a denser powder phase, displays a clear influence of  
154 the powder in the inter-pellet porosity whereas that of the 70/15 material, characterised by a loose  
155 powder phase, is not influenced by powder. These results suggest that powder can freely swell in the  
156 inter-pellet porosity until it reaches a volume fraction allowing powder grains to participate in the  
157 mechanical behaviour of the mixture.

158 In fully saturated state, an estimation of the final swelling pressure of MX80 bentonite-based  
159 materials from their dry density is proposed by Wang et al. (Wang et al., 2012). For the three studied  
160 materials, this estimation, obtained from empirical results on compacted powder samples, yields  
161 swelling pressures of 4.44 MPa, 0.970 MPa, and 0.210 MPa for the 70/30, 70/15, and 70/0 materials.  
162 The measured values are 4.45 MPa, 0.910 MPa, and 0.247 MPa, respectively. The close values  
163 compared to experimental results obtained on pellet mixtures suggest that a high degree of  
164 homogenisation is reached in the final state at the laboratory scale (Hoffmann et al., 2007; Imbert and  
165 Villar, 2006; van Geet et al., 2005), which is confirmed by sample dismantling (Figure 5).

a)



b)



166 Figure 5: Pictures of SP0 samples. a) SP0a at 9 MPa of suction, b) SP0b following liquid water saturation. The cell  
167 diameter is 60 mm.

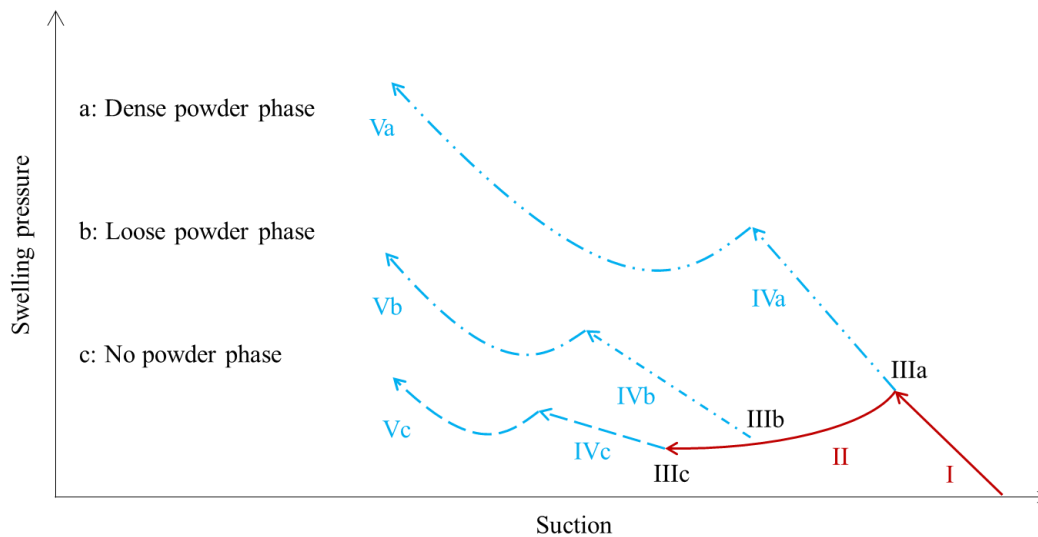
### 168 2.3.3. Conceptual interpretation of the material behaviour

169 Experimental results highlight that the material behaviour is controlled by the initial granular  
170 structure until powder volume fraction  $\Phi_2$  reaches a maximum value. For the 70/30 material (with  
171  $\Phi_{I0} = 0.553$ ), it occurs at  $s \approx 60$  MPa. Besides, all materials, including the 70/0 material, appear to  
172 have reached a high degree of homogenisation in the fully saturated state. In pellet assemblies, the  
173 influence of initial granular structure is lost between  $s = 4$  MPa and  $s = 0$  MPa. In this suction range, it  
174 has been evidenced that a significant reorganisation of the material fabric occurs (Saiyouri et al., 2004,  
175 2000). Aggregates exfoliation in the macroporosity occurs, the microstructure and hydration  
176 mechanisms change, and it is suggested that the initial granular structure no longer controls the  
177 macroscopic behaviour. The key phenomena controlling the behaviour of pellet-powder materials are  
178 thus: (i) the pellet stiffness; (ii) the pellet strength; (iii) a threshold value of  $\Phi_2$ ; (iv) a threshold value  
179 of  $s$ ; and (v) the behaviour of the material when the influence of the initial granular structure is lost.

180 A conceptual diagram describing the understanding of the material behaviour in the light of  
181 experimental results is presented in Figure 6. In this Figure, a wetting phase (decrease of suction) is  
182 represented for three types of pellet-powder mixtures (no powder, loose powder phase, dense powder  
183 phase).

184 Upon suction decrease, the swelling pressure evolution is first controlled by the assembly of pellets  
185 only (Phases I and II in Figure 6). During this phase, the material behaves as a granular assembly.  
186 Then, a “granular-continuous” transition is observed: the material response is not totally controlled by  
187 the granular structure anymore but still is not that of a continuous bentonite material (Phase III).  
188 Finally, the initial granular structure has lost its influence on the macroscopic response (Phases IV and  
189 V). During this “continuous phase”, the macroscopic response is controlled by the hydration of the  
190 bentonite regardless of the initial granular nature of the material.

191 Peak phenomena can be observed in the granular phase, as a consequence of the contact force  
192 reaching pellet strength, or in the continuous phase, as a result of the collapse of the macrostructure of  
193 the bentonite following microstructural rearrangement (Lloret et al., 2003).



194

Granular domain	I	Increase of contact forces
	II	Contact forces reach pellet strength
Transition	III	Loss of influence of the initial granular structure
Continuous domain	IV	Microstructural rearrangements and subsequent collapse of the macrostructure of the bentonite
	V	Increase of swelling pressure to the final value

195

196 Figure 6: Conceptual interpretation of the behaviour of pellet-powder materials upon hydration in constant-volume  
 197 conditions. The red solid lines represent the influence of the initial granular structure. The blue dashed lines represent the  
 198 behaviour after the transition to the continuous domain.

199

### 200 3. Insight into the behaviour of the granular material using DEM

201

#### 202 3.1. Objectives

203 Existing modelling framework used to describe the behaviour of compacted bentonite materials do  
 204 not account for the features described in the previous section. Since the pellet assembly can control the  
 205 mechanical response of the material if  $\Phi_2$  is below a threshold value, it is proposed in the present  
 206 section to study the mechanical behaviour of pellet assemblies with no powder.

207 In this respect, DEM is used to address the mechanical behaviour of pellet assemblies from the  
 208 mechanical properties of the pellet (Darde et al., 2018).

209

## 210 3.2. Method

211 DEM is used to perform isotropic compression on large pellet assemblies unaffected by cell walls  
212 to address the intrinsic behaviour of the material. Each pellet is modelled by a spherical particle. The  
213 behaviour of each particle, interaction at contacts and details concerning the simulation procedure are  
214 given in the following sections.

215

### 216 3.2.1. Model for a pellet at high suctions

217 (Darde et al., 2018) proposed, from experimental characterisation, the following expressions to  
218 describe the evolution of the pellet Young modulus,  $E_1$ , volumetric strain,  $\varepsilon_{V1}$ , and compressive  
219 strength,  $R_1$ :

$$E_1 = 3(1 - 2\nu_1) \frac{1}{\beta_m} \exp(\alpha_m p') \quad (1)$$

$$\varepsilon_{V1} = \int_{p'_0}^{p'} \beta_m \exp(-\alpha_m p') dp' \quad (2)$$

$$R_1 = C_A E_1 = 3(1 - 2\nu_1) \frac{C_A}{\beta_m} \exp(\alpha_m p') \quad (3)$$

$$p' = p + s \quad (4)$$

220 where  $\nu_1$  is the pellet Poisson ratio,  $p'$  is the effective mean stress,  $p'_0$  is the initial effective mean  
221 stress,  $C_A$ ,  $\alpha_m$  and  $\beta_m$  are model parameters,  $p$  is the total mean stress and  $s$  the total suction.

222 The model is based on the following assumptions: the pellet is considered saturated, its behaviour  
 223 is elastic and controlled by the behaviour of the aggregates. Further information and discussions  
 224 concerning the model can be found in (Darde et al., 2018). The values of the model parameters are  
 225 presented in Table 4.

226 Table 4: Parameters of the model for a pellet.

Parameter	Value
$\alpha_m$	0.024 MPa <sup>-1</sup>
$\beta_m$	0.016 MPa <sup>-1</sup>
$\nu_1$	0.3
$C_A$	1.206 x10 <sup>-7</sup> m <sup>-2</sup>
$s_0$	89 MPa

227

### 228 3.2.2. Contact laws

229 In DEM simulations, each pellet is modelled as a sphere. Interactions at contact between spheres  
 230 are described by (i) the Hertz law (equation (5)) for normal force with perfect plasticity as the normal  
 231 force  $F_N$  reaches the pellet strength  $R_f$  (Darde et al., 2020a) and (ii) a simplified form of the Cattaneo-  
 232 Mindlin-Deresiewicz law (Johnson, 1985) for tangential elasticity with sliding as the tangential force  
 233 reaches the Coulomb condition (Agnolin and Roux, 2007). Damping in contacts is considered as in  
 234 (Agnolin and Roux, 2007).

235 For two spheres of same diameter  $a$  in contact, the Hertz law is expressed as follows:

$$F_N = \frac{1}{3} \frac{E_1}{1 - \nu_1^2} a^{\frac{1}{2}} \delta_N^{\frac{3}{2}} \quad (5)$$

236 Where  $\delta_N$  is the normal deflection.

237

238 3.2.3. Study of the behaviour of large pellet assemblies under isotropic compression

239 (Darde et al., 2020a) highlighted that wall effects in the laboratory affect the material behaviour, as  
240 suggested by (Bernachy-barbe et al., 2020) in an experimental study. Thus, it is proposed to model  
241 large periodic pellet assemblies (with no wall) to address the intrinsic behaviour of these materials.  
242 The main objective is to determine constitutive laws describing the macroscopic response of pellet  
243 assemblies under variations of mean stress and suction. The macroscopic response of the material  
244 depends on pellet stiffness, pellet strength, pellet diameter (varying upon pellet swelling/shrinkage),  
245 deflection in contacts. All of them depend on both mean stress and suction. It is proposed to study: (i)  
246 the behaviour of the granular assembly under isotropic compression at constant sphere diameter; and  
247 (ii) the behaviour of the granular assembly under particle swelling at constant mean stress, pellet  
248 stiffness and pellet strength.

249 The behaviour of the granular assembly under isotropic compression at constant sphere diameter is  
250 studied using DEM. The behaviour of the granular assembly under particle swelling at constant mean  
251 stress, pellet stiffness and pellet strength is addressed through a theoretical approach, discussed in a  
252 forthcoming section.

253 Two dimensionless control parameters are used in DEM simulations. A dimensionless pressure  
254 parameter,  $m_g$ , is used to describe the compression state of the granular assembly.  $m_g$  is defined as:

$$m_g = \left( \frac{p}{\frac{E_1}{1 - \nu_1^2}} \right)^{\frac{2}{3}} \quad (6)$$

255 Where  $p$  is the mean stress in the granular assembly. Details concerning the expression of  $m_g$  can  
256 be found in Appendix A.

257  $m_g$  is a convenient parameter to study the behaviour of the pellet assembly, since a single term  
258 depending on both mean stress and pellet stiffness can account for features such as deflection in  
259 contacts, creation/loss of contacts between pellets, evolution of the total volume (see Appendix A).

260 The strain rate of the periodic cell,  $\dot{\epsilon}$ , is controlled by a dimensionless inertia parameter,  $I$ , defined  
 261 as (Agnolin and Roux, 2007):

$$I = \dot{\epsilon} \left( \frac{m_1}{a p} \right)^{\frac{1}{2}} \quad (7)$$

262 where  $m_1$  is the mass of the pellet.

263 A constant value of  $I$  is imposed to apply a constant strain rate of the cell. In the present work,  $I$  is  
 264 set to  $10^{-5}$  to model an isotropic compression at constant slow rate. The evolution of  $m_g$  is determined  
 265 from equation (6) during compression.

266 The simulations are performed on different granular assemblies, prepared at different values of  $\Phi_{10}$   
 267 and initial coordination number  $Z$ . All numerical samples are composed of 4000 spheres, in a cubic  
 268 cell with periodic boundary conditions (pellets located at one cell boundary are in contact with pellets  
 269 located at the opposite boundary), thus no pellet-wall interaction exists (Agnolin and Roux, 2007).  
 270 Five types of granular assemblies are prepared and denoted A, B, C, D, and E. For each type of  
 271 granular assembly, three samples are prepared to assess the calculation repeatability. A, B, C, and E  
 272 samples are prepared under  $m_g = 1.19 \times 10^{-4}$ ; D samples are prepared under  $m_g = 1.03 \times 10^{-4}$ . Samples  
 273 preparation procedure is described in details in (Agnolin and Roux, 2007). Table 5 summarises the  
 274 main initial properties of the samples.

275 Table 5: Initial properties of the numerical samples. All samples are cubic and contain 4000 spheres.

Sample		$Z$	$\Phi_{10}$
A	1	6.0	0.638
	2	6.1	0.639
	3	6.0	0.636
B	1	4.4	0.636
	2	4.2	0.634

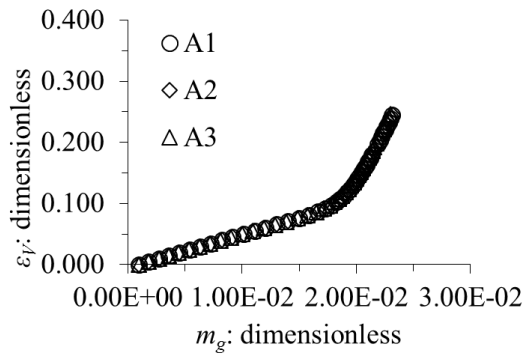
		3	4.3	0.635
	C	1	4.4	0.595
		2	4.3	0.593
		3	4.4	0.594
	D	1	4.5	0.577
		2	4.4	0.575
		3	4.4	0.578
	E	1	5.8	0.628
		2	5.8	0.627
		3	5.8	0.627

276

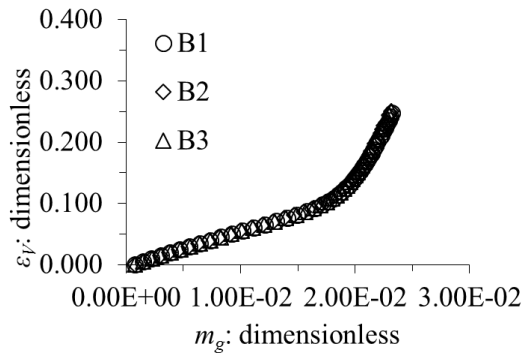
277 **3.3. DEM simulation results and discussion**

278 The evolution of volumetric strain, denoted by  $\varepsilon_V$ , during isotropic compression is presented in  
 279 Figure 7 as a function of  $m_g$ , for all the granular assemblies. Compressive stress are positive and  
 280 positive volumetric strains are associated to volume decrease in the following.

a)

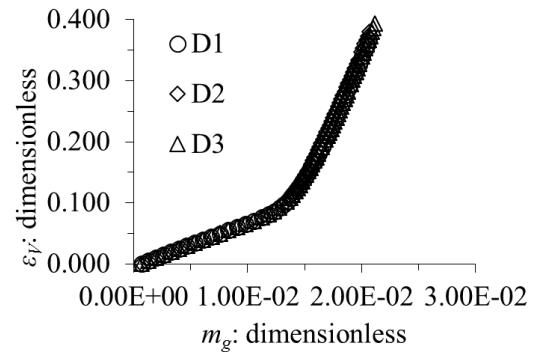
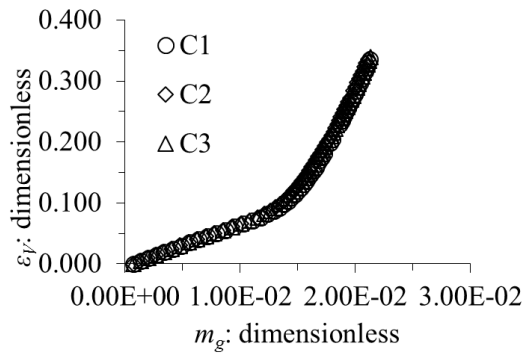


b)

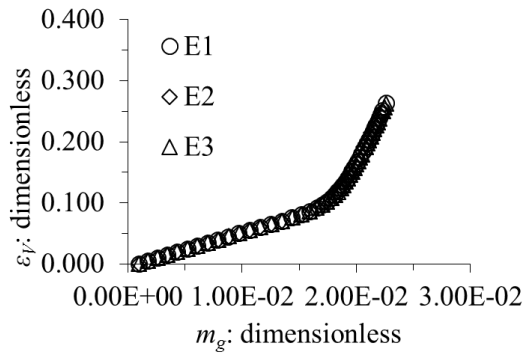


c)

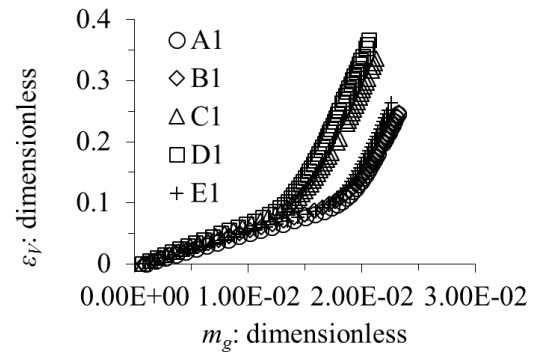
d)



e)



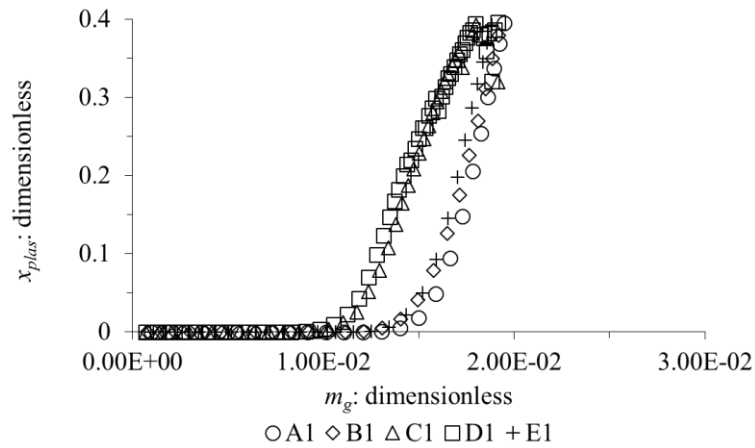
f)



281

282 Figure 7: Evolution of  $\varepsilon_V$  as a function of  $m_g$  during isotropic compression for all granular assemblies. a) A samples, b) B  
 283 samples, c) C samples, d) D samples, e) E samples, f) comparison between A1, B1, C1, D1, E1.

284 All granular assemblies display a comparable response during isotropic compression. The relation  
 285 between  $\varepsilon_V$  and  $m_g$  can be represented by a piecewise linear function with two pieces. As highlighted  
 286 in Figure 7f, the slopes  $\Delta\varepsilon_V/\Delta m_g$  do not vary significantly from one sample to another. The threshold  
 287 value of  $m_g$  varies depending on the sample types, however.



288

289

Figure 8: Comparison of the evolution of  $x_{plas}$  as a function of  $m_g$  for the five types of granular assemblies.

290

291

292

293

294

From the definition of  $m_g$  (equation (6)) and results presented in Figure 7, the influence of pellet stiffness and mean stress is easily determined. Increase in  $p$  at constant  $E_I$  causes the total volume to decrease. Decrease in  $E_I$  at constant  $p$  causes the total volume to decrease. For  $E_I$  increasing with increasing  $p$  (equations (1) and (4)), evolution of  $p$  can induce competing effects on the total volumetric strain, which highlights the relevance of  $m_g$  to describe the material behaviour.

295

296

297

298

299

300

301

302

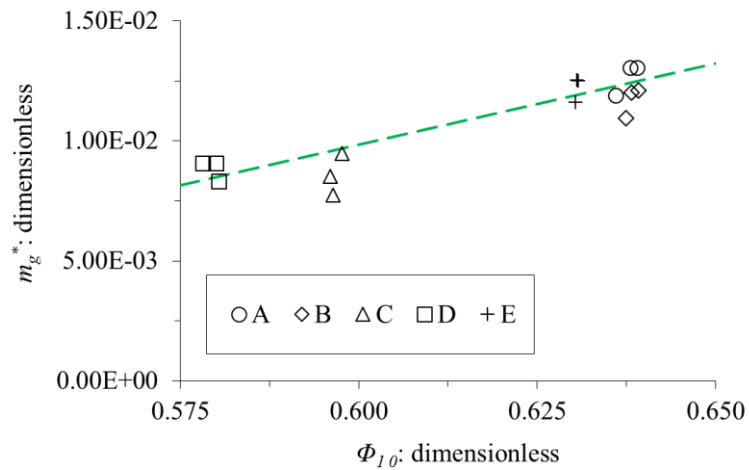
The pellet strength is accounted for by introducing perfect plasticity in the contact law. Influence of the pellet strength is thus highlighted by comparison of the evolutions of  $\varepsilon_V$  and the proportion of plastic contacts,  $x_{plas}$ , as functions of  $m_g$  during isotropic compression (Figure 7 and Figure 8). In all samples, all contacts remain elastic until a threshold value of  $m_g$  is reached. Contact plasticity then increases continuously. Interestingly, this threshold value is very close to that corresponding to the slope change in the piecewise linear evolution of  $\varepsilon_V(m_g)$ . This limit value of  $m_g$  is denoted by  $m_g^*$ . The slope change in the  $\varepsilon_V$ - $m_g$  relationship is interpreted as a consequence of contact forces reaching the pellet strength.

303

304

305

From Figure 7, it is highlighted that  $\Phi_{10}$  has no significant influence on the values of  $\Delta\varepsilon_V/\Delta m_g$ . Figure 8 however highlights that  $m_g^*$  is higher for higher values of  $\Phi_{10}$ . The relationship between these two values is plotted in Figure 9 for all samples.



306

307 Figure 9: Relationship between  $m_g^*$  and  $\Phi_{10}$  for all samples. The dashed line represents the fit corresponding to

308  $m_g^* = 0.067 \Phi_{10} - 0.031$ .

309

#### 310 4. Proposition of a macroscopic model for pellet-powder mixtures

311

##### 312 4.1. Conceptual approach

313 This section presents a conceptual model able to describe the hydromechanical behaviour of pellet-  
 314 powder mixtures, accounting for relevant features such as a free swelling phase for the powder,  
 315 influence of granular structure, influence of pellet strength, transition to a continuous state. The  
 316 approach is based on the scheme presented in Figure 6.

317 Following this approach, the material is considered to be either “granular” or “continuous”. In the  
 318 granular domain, the mechanical behaviour is controlled by the pellet assembly. Constitutive laws are  
 319 proposed from DEM results. In the continuous domain, the material behaves as a continuum. Its  
 320 mechanical behaviour is described by a modified Barcelona Basic Model (BBM, (Alonso et al.,  
 321 1990)). Transition from granular domain to continuous domain is related to a ratio of powder volume  
 322 fraction to pellet volume fraction and to suction.

323 Three different pore types are considered: the pellet void ratio is denoted by  $e_1$ ; the powder grains  
 324 void ratio is denoted by  $e_2$ ; and the total void ratio is denoted by  $e$ :

$$e_1 = \frac{\Omega_{v1}}{\Omega_{s1}} \quad (8)$$

$$e_2 = \frac{\Omega_{v2}}{\Omega_{s2}} \quad (9)$$

$$e = \frac{\Omega_v}{\Omega_s} \quad (10)$$

325 where  $\Omega_{s1}$  and  $\Omega_{s2}$  are the volume of solid in the pellets and powder grains, and  $\Omega_s = \Omega_{s1} + \Omega_{s2}$  is the  
 326 total volume of solid in the mixture.  $\Omega_{v1}$  and  $\Omega_{v2}$  are the volume of void in the pellets and powder  
 327 grains (microstructural pores), and  $\Omega_v$  is the total volume of voids in the mixture. Denoting by  $\Omega_{vM}$  the  
 328 volume of void between pellets and powder grains (macrostructural pores,  $\Omega_{vM} = \Omega_v - \Omega_{v1} - \Omega_{v2}$ ), the  
 329 macrostructural void ratio,  $e_M$ , is defined as:

$$e_M = \frac{\Omega_{vM}}{\Omega_s} \quad (11)$$

330 The microstructural void ratio,  $e_m$ , is then defined as:

$$e_m = \frac{\Omega_{s1}}{\Omega_s} e_1 + \frac{\Omega_{s2}}{\Omega_s} e_2 \quad (12)$$

331 The solid phase is considered incompressible. In all the formulation, volumetric strains are defined  
 332 relative to the initial volume. Volumetric strains associated to each levels of structure are defined as  
 333 follows:

$$\varepsilon_{v1} = -\frac{\Delta e_1}{1 + e_{10}} \quad (13)$$

$$\varepsilon_{V2} = -\frac{\Delta e_2}{1 + e_{20}} \quad (14)$$

$$\varepsilon_V = -\frac{\Delta e}{1 + e_0} \quad (15)$$

334 where  $\varepsilon_{V1}$  and  $\varepsilon_{V2}$  are the volumetric strains of the pellets and of the powder grains, respectively. The  
 335 initial value of  $e$ ,  $e_1$ ,  $e_2$ , are denoted by  $e_0$ ,  $e_{10}$ ,  $e_{20}$ , respectively.

336 Volume fractions of the different levels of structure are defined as follows:

$$\phi_1 = \frac{\Omega_{v1} + \Omega_{s1}}{\Omega_v + \Omega_s} \quad (16)$$

$$\phi_2 = \frac{\Omega_{v2} + \Omega_{s2}}{\Omega_v + \Omega_s} \quad (17)$$

$$\phi_M = 1 - \phi_1 - \phi_2 \quad (18)$$

337 where  $\phi_1$ ,  $\phi_2$ ,  $\phi_M$  are the volume fractions of pellets, powder, and macrostructural voids. For  
 338 convenience, an additional volume fraction,  $\phi_{mat}$ , is considered.  $\phi_{mat}$  is the volume fraction of the  
 339 granular assembly composed of the powder grains within inter-pellet voids:

$$\phi_{mat} = \frac{\Omega_{v2} + \Omega_{s2}}{\Omega - (\Omega_{v1} + \Omega_{s1})} = \frac{\phi_2}{1 - \phi_1} \quad (19)$$

340 Suction in pellets is denoted by  $s_1$ , suction in powder is denoted by  $s_2$ , suction in macropores is  
 341 denoted by  $s_M$ . In the conceptual approach presented in this study, hydraulic equilibrium is considered:

$$s_1 = s_2 = s_M = s \quad (20)$$

342 The macroscopic mean stress  $p$  is parted into two terms affecting the pellet and powder phases as  
 343 follows:

$$p = \sum_i \phi_i p_i \quad (21)$$

344 And the effective mean stress in each phase  $i$ ,  $p'_i$  is defined as follows:

$$p'_i = s_i + p_i \quad (22)$$

345 where  $\phi_i$ ,  $p_i$  and  $s_i$  are the volume fraction of phase  $i$ , mean stress in phase  $i$  and suction in phase  $i$ ,  
 346 respectively.

347 In the granular domain, it is assumed that the pellet controls the mechanical behaviour of the  
 348 material, as observed in swelling pressure tests. Only pellets are affected by the macroscopic mean  
 349 stress. Thus, effective mean stresses in the granular domain are defined as follows:

$$p'_1 = s + \frac{p}{\phi_1} \quad (23)$$

$$p'_2 = s \quad (24)$$

350 In the continuous domain, it is assumed that both pellets and powder contribute to the mechanical  
 351 behaviour of the material. Effective mean stresses in the continuous domain are defined as follows:

$$p'_1 = s + \frac{p}{\phi_1 + \phi_2} \quad (25)$$

$$p'_2 = s + \frac{p}{\phi_1 + \phi_2} \quad (26)$$

352 Transition from granular to continuous domain occurs as the pellet assembly no longer controls the  
 353 mechanical behaviour of the pellet-powder mixture. From experimental results, it is proposed that this  
 354 phenomenon can be related to the density of the granular assembly composed of the powder grains  
 355 within inter-pellet voids. The following ratio  $r_{vf}$  is proposed to describe the density of the powder  
 356 phase:

$$r_{vf} = \frac{\phi_{mat}}{\phi_1} \quad (27)$$

357 A threshold value of  $r_{vf}$ , denoted by  $r_{vf}^*$ , has to be determined. The material is considered in the  
 358 continuous domain if the following condition is verified:

$$r_{vf} \geq r_{vf}^* \quad (28)$$

359 It was discussed in (Darde et al., 2020b, 2018) that the model used to study the behaviour of a  
 360 pellet assembly using DEM was no longer relevant at low suction. Indeed, bentonite materials undergo  
 361 significant microstructural changes at low suction that have an influence on the macroscopic response  
 362 under hydromechanical loadings (Molinero-Guerra et al., 2020; Saiyouri et al., 2004; Villar, 2007).  
 363 For instance, the significant increase of swelling pressure observed at suction lower than 4 MPa in the  
 364 swelling pressure tests, regardless of the powder content, (Figure 3) cannot be reproduced using the  
 365 DEM model. These phenomena are not related to the initial granular structure. Thus, in the proposed  
 366 conceptual approach, a threshold value of suction for the domain transition is proposed.

367 The threshold suction, denoted by  $s^*$ , is also a material parameter. The material is considered in the  
368 continuous domain if the following condition is verified:

$$s \leq s^* \quad (29)$$

369 The transition is related to the loss of the initial structure and is considered an irreversible  
370 phenomenon.

371

372 In both granular and continuous domains, the volumetric strain of the microstructure (pellets and  
373 powder grains) is considered to remain elastic. Plasticity only affects the macrostructure. In the  
374 granular domain, DEM results highlighted that local plasticity in contacts can affect the material  
375 behaviour. In the proposed approach, this phenomenon is addressed by considering different elastic  
376 stiffness parameters depending on the value of  $m_g$ . These points are presented in the following section.

377

#### 378 **4.2. Elastic volumetric strains**

379 In the granular domain, the increment of elastic (superscript (e)) volumetric strains for the  
380 microstructure (pellets and powder) grains are written as follows:

$$d\varepsilon_{V1}^{(e)} = d\varepsilon_{V1} = \beta_m \exp(-\alpha_m p'_1) dp'_1 \quad (30)$$

381 and

$$d\varepsilon_{V2}^{(e)} = d\varepsilon_{V2} = \beta_m \exp(-\alpha_m p'_2) dp'_2 \quad (31)$$

382 As previously discussed, in the granular domain the behaviour of the granular assembly is  
 383 considered to be dependent on variations of  $m_g$  (equation (15)) at constant pellet volume and variations  
 384 of pellet volume at constant  $m_g$ . Elastic total volumetric strain is thus a function of  $m_g$  and  $\varepsilon_{V1}$ :

$$d\varepsilon_V^{(e)} = \frac{\partial \varepsilon_V^{(e)}}{\partial m_g} dm_g + \frac{\partial \varepsilon_V^{(e)}}{\partial \varepsilon_{V1}} d\varepsilon_{V1} \quad (32)$$

385 Denoting  $\frac{\partial \varepsilon_V^{(e)}}{\partial m_g}$  by  $f_\varepsilon$  and  $\frac{\partial \varepsilon_V^{(e)}}{\partial \varepsilon_{V1}}$  by  $f_{Mm}$ , equation (32) is written as follows:

$$d\varepsilon_V^{(e)} = f_\varepsilon dm_g + f_{Mm} d\varepsilon_{V1} \quad (33)$$

386 where  $f_\varepsilon$  is the slope of the piecewise linear function as discussed in the DEM study:

$$\begin{cases} f_\varepsilon = f_{\varepsilon a} ; m_g \leq m_g^* \\ f_\varepsilon = f_{\varepsilon b} ; m_g > m_g^* \end{cases} \quad (34)$$

387 in which  $f_{\varepsilon a}$  and  $f_{\varepsilon b}$  are parameters, with  $f_{\varepsilon a} < f_{\varepsilon b}$ .  $m_g^*$  is a function of the initial volume fraction of  
 388 pellets  $\phi_{10}$  (Figure 9):

$$m_g^* = f_{m a} \phi_{10} + f_{m b} \quad (35)$$

389 with  $f_{m a}$  and  $f_{m b}$  two model parameters. Equations (34) and (35) allow to account for contact plasticity  
 390 in the model while still considering the stress state to be elastic.

391  $f_{Mm}$  is obtained from equations (5) and (56) (Appendix A). For elastic contacts, its value is 1 in a  
 392 granular assembly of spherical particles. See details in Appendix B.

393 Constitutive models for unsaturated soils generally consider two independent stress variables. In  
 394 the present work, this approach is adopted and the two stress variables used to describe the volumetric

395 behaviour are the mean stress  $p$  and suction  $s$ . In this respect, an alternative expression for equation  
 396 (33) is:

$$d\varepsilon_V^{(e)} = \left( f_\varepsilon \frac{\partial m_g}{\partial p} + f_{Mm} \frac{\partial \varepsilon_{V1}}{\partial p} \right) dp + \left( f_\varepsilon \frac{\partial m_g}{\partial s} + f_{Mm} \frac{\partial \varepsilon_{V1}}{\partial s} \right) ds \quad (36)$$

397

398 with

$$\frac{\partial m_g}{\partial p} = \frac{2}{3} \left[ \frac{1}{p} - \frac{\alpha_m}{\phi_1} \right] \left( \frac{\beta_m}{3} \frac{1 - \nu^2}{1 - 2\nu} \right)^{\frac{2}{3}} p^{\frac{2}{3}} \exp\left(-\frac{2}{3} \alpha_m p'_1\right) \quad (37)$$

$$\frac{\partial m_g}{\partial s} = -\frac{2}{3} \alpha_m \left( \frac{\beta_m}{3} \frac{1 - \nu^2}{1 - 2\nu} \right)^{\frac{2}{3}} p^{\frac{2}{3}} \exp\left(-\frac{2}{3} \alpha_m p'_1\right) \quad (38)$$

$$\frac{\partial \varepsilon_{V1}}{\partial p} = \frac{\beta_m}{\phi_1} \exp(-\alpha_m p'_1) \quad (39)$$

$$\frac{\partial \varepsilon_{V1}}{\partial s} = \beta_m \exp(-\alpha_m p'_1) \quad (40)$$

399

400 In the continuous domain, the BBM (Alonso et al., 1990) is modified to account for three distinct  
 401 porosities. Increment of elastic volumetric strains are written as follows:

$$d\varepsilon_{V1}^{(e)} = d\varepsilon_{V1} = \frac{\kappa_m}{1 + e_{10}} \frac{dp'_1}{p'_1} \quad (41)$$

402 and

$$d\varepsilon_{V2}^{(e)} = d\varepsilon_{V2} = \frac{\kappa_m}{1 + e_{20}} \frac{dp'_2}{p'_2} \quad (42)$$

403 where  $\kappa_m$  is a dimensionless stiffness parameter.

404 Elastic total volumetric strain is a function of the volumetric strains of each level of structure:

$$d\varepsilon_V^{(e)} = \frac{1}{1 + e_0} \left[ (1 + e_{M0}) d\varepsilon_{VM}^{(e)} + (1 - x_s)(1 + e_{10}) d\varepsilon_{V1} + x_s (1 + e_{20}) d\varepsilon_{V2} \right] \quad (43)$$

405 where  $e_{M0}$  is the initial value of  $e_M$ ,  $\varepsilon_{VM}^{(e)}$  is the elastic volumetric strain of the macrostructure  
 406 (macropores between pellets and powder grains) and  $x_s$  is defined as:

$$x_s = \frac{\Omega_s}{\Omega_s} \quad (44)$$

407 The elastic increment of macrostructure volumetric strain is defined as follows:

$$d\varepsilon_{VM}^{(e)} = \frac{1}{1 + e_{M0}} \left( \kappa \frac{dp}{p} + \kappa_s \frac{ds}{s + p_{atm}} \right) \quad (45)$$

408 where  $\kappa$  and  $\kappa_s$  are dimensionless stiffness parameters related to variations of  $p$  and  $s$ , respectively, and  
 409  $p_{atm}$  is the atmospheric pressure.

410 The dependency of the macrostructural swelling potential on the material density is accounted for  
 411 by assuming a linear relationship between  $\kappa_s$  and  $\kappa_m$ :

$$\kappa_s = \frac{e_{m0}}{e_0} \kappa_m \quad (46)$$

412 where  $e_{m0}$  is the initial value of  $e_m$ .

413

### 414 4.3. Plasticity and hardening

415 A single plastic flow rule is used for the granular and continuous domains. Plasticity and hardening  
416 are addressed using the concept of the Loading-Collapse curve (Alonso et al., 1990). The elastic limit  
417  $p^*$  evolves as a function of suction as:

$$p^*(s) = p_c \left( \frac{p^*(0)}{p_c} \right)^{\frac{\lambda(0)-\kappa}{\lambda(s)-\kappa}} \quad (47)$$

418 where  $p_c$  is the BBM reference stress (Alonso et al., 1990) and  $\lambda(s)$  is a dimensionless elastoplastic  
419 stiffness parameter, function of  $s$ . The hardening law is written as follows:

$$\frac{dp^*(0)}{p^*(0)} = \frac{1 + e_0}{\lambda(0) - \kappa} d\varepsilon_v^{(p)} \quad (48)$$

420 where the superscript (p) denotes the plastic part of the volumetric strain.

421 The evolution of the dimensionless elastoplastic stiffness parameter  $\lambda$  as a function of suction is  
422 described as follows:

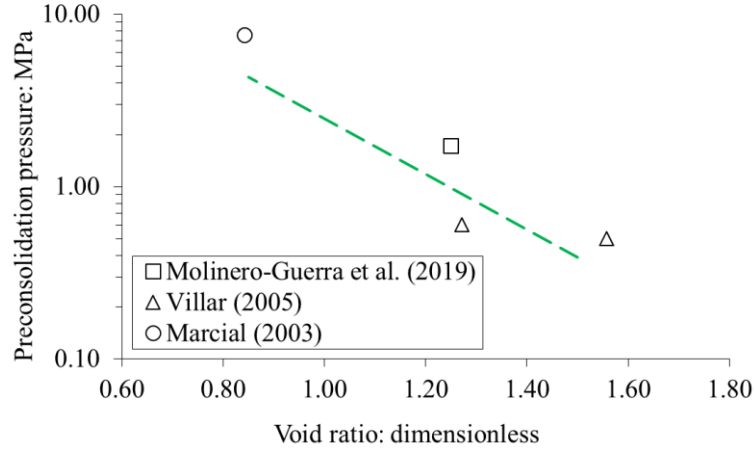
$$\lambda(s) = \lambda_0 [\rho + (1 - \rho) \exp(-\omega s)] \quad (49)$$

423 where  $\lambda_0$ ,  $\rho$ , and  $\omega$  are material parameters respectively related to the saturated elastoplastic stiffness,  
424 ratio of  $\lambda(s \rightarrow \infty)$  to  $\lambda(0)$ , and evolution of stiffness with suction.

425 From oedometer tests carried out on saturated MX80 bentonite materials by (Marcial, 2003;  
426 Molinero-Guerra et al., 2019a; Villar, 2005), an empirical relationship between the initial value of  
427  $p^*(0)$  and  $e_0$  is proposed (Figure 10):

$$p^*(0) = p_r \exp(-n_p e_0) \quad (50)$$

428 where  $p_r$  is a reference stress and  $n_p$  a material parameter.



429

430 Figure 10: Preconsolidation pressure as a function of the void ratio in oedometer tests performed on bentonite materials  
 431 by Molinero-Guerra et al. (2019) (Molinero-Guerra et al., 2019a), Villar (2005) (Villar, 2005), and Marcial (2003) (Marcial,  
 432 2003). The green dashed line is obtained using equation (50) with  $p_r = 80$  MPa and  $n_p = 3.7$ .

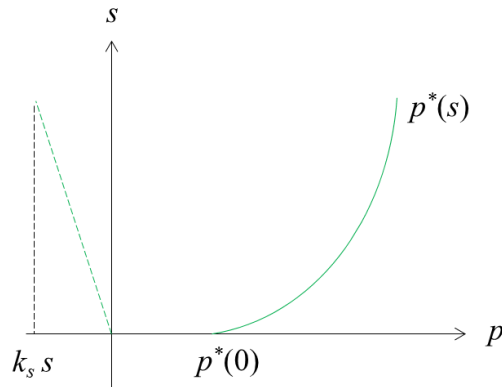
433 In triaxial stress states, the yield surface is written as in the original BBM:

$$q^2 - M^2(p + k_s s)(p^*(s) - p) = 0 \quad (51)$$

434 where  $q$  is the deviatoric stress,  $M$  is the slope of the critical state line, and  $k_s$  a parameter related to the  
 435 increase in cohesion with increasing suction (Alonso et al., 1990). An associated flow rule is  
 436 considered in the model.

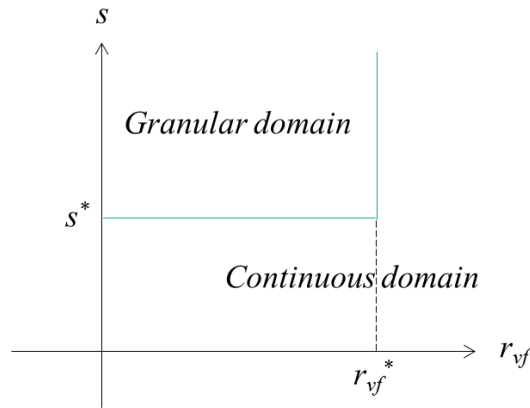
437 A sketch of the elastic domain in the  $p$ - $s$  plane is presented in Figure 11. A summary of the model  
 438 equations for volumetric strains is presented in Table 6.

439 a)



440

441 b)



442

443 Figure 11: Sketch of the model elastic domain: a) in the  $p$ - $s$  plane, b) partition of the elastic domain in the granular and  
 444 continuous domains.

445 Table 6: Summary of the model equations related to the volumetric strains.

			Granular domain	Continuous domain
Pellet	$\varepsilon_{V1}$	elastic	Equation (30)	Equation (41)
		plastic	only elastic	only elastic
Powder grains	$\varepsilon_{V2}$	elastic	Equation (31)	Equation (42)
		plastic	only elastic	only elastic
Granular assembly	$\varepsilon_V$	elastic	Equation (33)	Equation (43)
		plastic	Equations (47) to (51)	Equations (47) to (51)

446

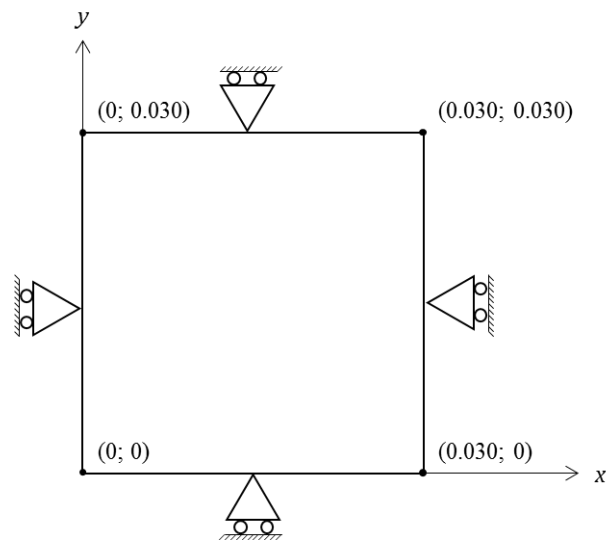
## 447 5. Simulations of swelling pressure tests

448 The model is implemented in the open source finite element method (FEM) code Bil developed by  
449 Dangla (Dangla, 2018). The swelling pressure tests carried out in the laboratory are simulated using  
450 the model to assess its ability to reproduce the behaviour of pellet-powder mixture.

451

### 452 5.1. Method

453 The swelling pressure tests are modelled using two-dimensional axisymmetric conditions. The  $y$   
454 axis is the axis of symmetry. The mesh consists in one Q4 element. This latter is presented in Figure  
455 12.



456

457 Figure 12: Geometry of the FEM simulations. Lengths are given in m.

458 The following initial conditions for the displacement field,  $\mathbf{u}$ , initial stress state and suction are  
459 used in all the simulations, for the three swelling pressure tests:

460 -  $\mathbf{u} = 0$ ;

461 -  $s_0 = 89 \text{ MPa}$ ;

462 -  $\sigma_{xx 0} = 10^{-5} \text{ MPa}$ ;

463 -  $\sigma_{yy 0} = 10^{-5}$  MPa;

464 -  $\sigma_{zz 0} = 10^{-5}$  MPa.

465 where  $\sigma_{xx 0}$ ,  $\sigma_{yy 0}$  and  $\sigma_{zz 0}$  are the initial diagonal components of the Cauchy stress tensor. Initial mean  
466 stress is taken higher than zero to avoid numerical issues associated to zero stress. Gravity is not  
467 considered in the simulations. The initial suction in the simulations is taken equal to the pellet initial  
468 suction, considered more representative of the whole system than that of the powder.

469 The boundary conditions used in the simulations are:

470 -  $u_y = 0$  on the top boundary ( $y = 0.030$  m);

471 -  $u_y = 0$  on the bottom boundary ( $y = 0$ );

472 -  $u_x = 0$  on the left boundary ( $x = 0$ );

473 -  $u_x = 0$  on the right boundary ( $x = 0.030$  m).

474 For simplicity,  $p_{atm}$  is taken equal to zero and  $s$  is progressively decreased from 89 MPa to 0.1 MPa  
475 such that  $s + p_{atm}$  is still equal to atmospheric pressure in the final state (equation (45)).

476 The parameters required for the simulations are mixture properties, elastic parameters in the  
477 granular domain, elastic parameters in the continuous domain, domain transition parameters, and  
478 plasticity parameters. These latter are obtained from the laboratory tests, DEM periodic simulations,  
479 literature or estimation if not available.

480 Mixture properties obtained from experimental characterisation are shown in Table 7. Parameters  
481 related to the elastic behaviour are recapitulated in Table 8. Parameters related to the granular domain  
482 are from (Darde et al., 2018) and DEM simulations presented in a previous section.  $\kappa$  is chosen in the  
483 same range as the dimensionless elastic stiffness parameter proposed by (Mokni et al., 2020) for a  
484 MX80 bentonite pellet-powder mixture using the same pellets and powder. Parameters related to the  
485 granular to continuous transition are presented in Table 9. The threshold suction  $s^*$  is chosen according  
486 to experimental observations by (Saiyouri et al., 2004) and (Molinero-Guerra et al., 2020) that a  
487 significant microstructural rearrangement occurs in MX80 bentonite in the range 3-7 MPa of suction.

488 The value of  $r_{vf}^*$  is taken equal to 1. Parameters related to the plastic behaviour are presented in Table  
 489 10.  $\lambda_0$ ,  $\rho$  and  $\omega$  are taken in the same range as in (Mokni et al., 2020).  $p_r$  and  $n_p$  are obtained from  
 490 experimental results (Figure 10). The values of  $\kappa_m$  and  $p_c$  are estimated so that all swelling pressure  
 491 tests are satisfactorily simulated with a single set of parameters.

492 Table 7: Model parameters related to the mixture properties.

Property	70/0	70/15	70/30
$x_s$	0	0.18	0.30
$\phi_{10}$	0.553	0.553	0.553
$\phi_{mat0}$	0	0.275	0.529
$s_0$ : MPa	89	89	89
$e_{10}$	0.450	0.450	0.450
$e_{20}$	0.450	0.450	0.450
$e_{M0}$	1.19	0.722	0.396
$e_0$	1.64	1.17	0.847

493

494 Table 8: Model parameters related to the elastic behaviour of the material.

Elasticity parameters	All mixtures
<i>Granular domain</i>	
$\alpha_m$ : MPa <sup>-1</sup>	0.024
$\beta_m$ : MPa <sup>-1</sup>	0.016
$f_{Mm}$	1
$f_{\varepsilon a}$	6
$f_{\varepsilon b}$	40
$f_{m a}$	0.067
$f_{m b}$	-0.031

<i>Continuous domain</i>	
$\kappa$	0.025
$\kappa_m$	0.015

495

496

Table 9: Model parameters related to the granular-continuous transition.

Transition parameters	All mixtures
$s^*$ : MPa	3
$r_{vf}^*$	1

497

498

Table 10: Model parameters related to the plastic behaviour of the material.

Plasticity parameters	All mixtures
$\lambda_0$	0.20
$p_c$ : MPa	0.050
$\rho$	0.8
$\omega$ : MPa <sup>-1</sup>	0.1
$p_r$ : MPa	80
$n_p$	3.7

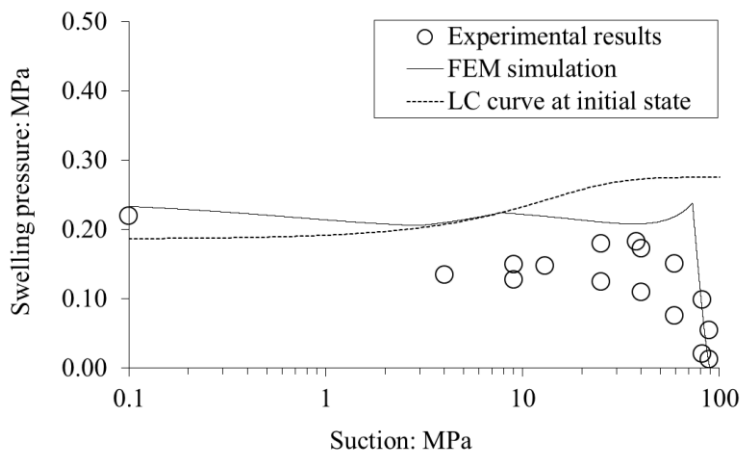
499

## 500 5.2. FEM simulation results

501 Figure 13a presents the comparison between experimental and numerical results for SP0a and SP0b  
502 tests. In the simulation, the swelling pressure increases then reaches a first peak corresponding to  
503 pellet strength. Following the peak, swelling pressure remains nearly constant until LC yielding occurs  
504 while in the granular domain. Following transition to continuous domain, the swelling pressure  
505 increases again to its final value as elastic swelling overcomes the plastic closure of macro-porosity.  
506 The general trend of the swelling pressure evolution as well as its order of magnitude are satisfactorily  
507 reproduced. The final swelling pressure in the simulation is close to the final swelling pressure in

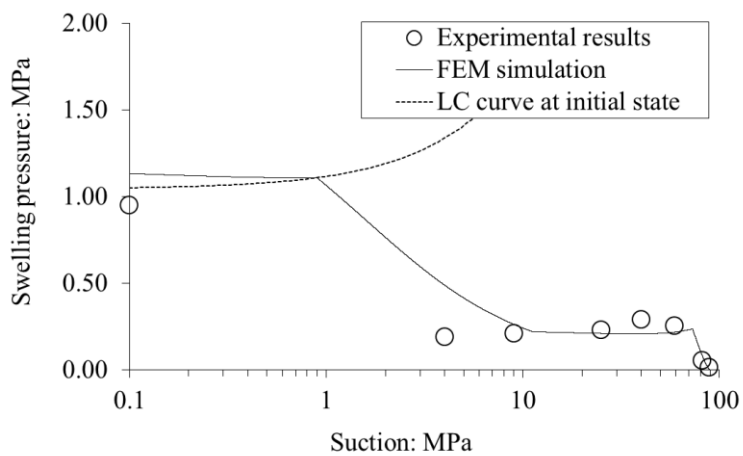
508 experiments. Some differences between experimental and numerical results still can be observed and  
509 are discussed in the next section.

510 a)



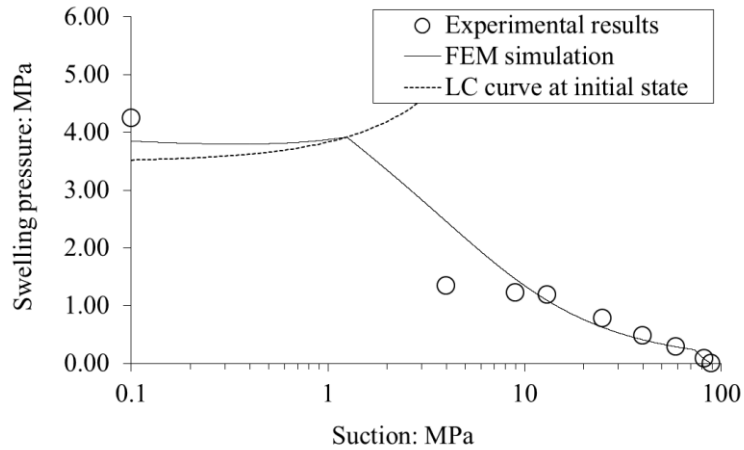
511

512 b)



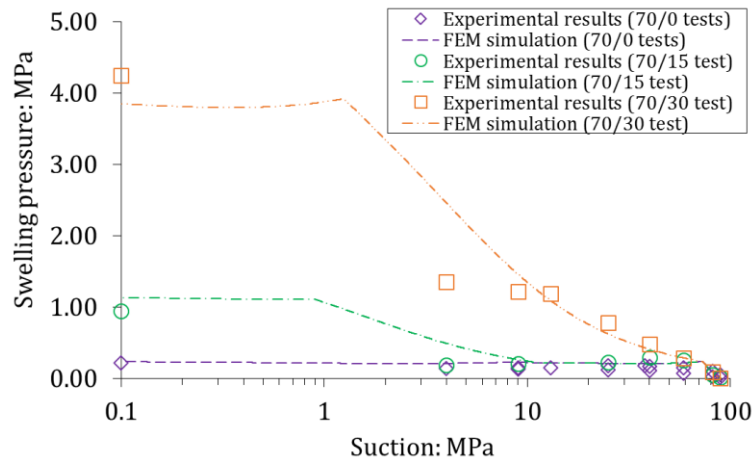
513

514 c)



515

516 d)



517

518 Figure 13: Comparison between FEM simulation and experimental results of swelling pressure tests for a) 70/0 material;  
 519 b) 70/15 material; c) 70/30 material, d) comparison of all FEM simulation and experimental results.

520 Figure 13b presents the comparison between experimental and numerical results for SP15 test. In  
 521 the simulation, the swelling pressure increases and reaches a peak as pellet strength is reached, then  
 522 remains nearly constant until suction reaches  $\sim 11$  MPa. At this point  $r_{vf}$  reaches 1 and the material is  
 523 considered continuous. Afterward, swelling pressure increases until reaching the LC yield locus. Then,  
 524 the swelling pressure remains nearly constant. The final swelling pressure in the simulation is  
 525 overestimated but still close to experimental results.

526 Figure 13c presents the comparison between experimental and numerical results for the 70/30  
 527 mixture. Transition occurs as  $r_{vf} = 1$  at high suction ( $\sim 70$  MPa in the simulation) and most of the

528 hydration occurs while in the continuous domain. Swelling pressure increases, then LC yielding  
529 occurs and the swelling pressure remains nearly constant and reaches a final value close to  
530 experimental results. It is interesting to note that, even simplified, the conceptual approach proposed  
531 for the continuous domain is able to reproduce the evolution of swelling pressure upon suction  
532 decrease.

533 A comparison of all numerical and experimental results is presented in Figure 13d. It is highlighted  
534 that the proposed conceptual approach is able to satisfactorily reproduce the mechanical behaviour of  
535 pellet-based bentonite materials upon suction decrease in constant-volume conditions, either with no  
536 powder or with powder of various densities in the inter-pellet voids, over a wide range of average dry  
537 densities ( $1.05 \text{ Mg/m}^3$  to  $1.50 \text{ Mg/m}^3$ ). Some differences were obtained between experimental results  
538 and prediction of the model, as previously mentioned. However, Figure 13d shows that both the  
539 general trends and amplitude of the swelling pressure evolution upon suction decrease are still  
540 comparable to the experimental results.

541

## 542 **6. Discussion**

543

### 544 **6.1. Hypotheses of the conceptual model**

545

#### 546 6.1.1. Distinction of two domains and transition criteria

547 A hypothesis of the model is the consideration of two distinct domains. The mixture is considered  
548 either granular, with powder having no contribution to the mechanical behaviour, or continuous, with  
549 pellet and powder equally contributing to the mechanical behaviour.

550 The swelling pressure in SP15 test was very close to, but still slightly higher than, SP0a and SP0b  
551 swelling pressure. Even if moderate, powder may have an influence in “loose powder phase” mixtures  
552 in the granular domain. The eventual remaining influence of the initial granular structure is not

553 considered when the material is in the continuous domain. It is not known how the evolution of the  
554 swelling pressure in SP30 test would compare to that of a compacted powder sample of same dry  
555 density. The final state, following water saturation, was homogeneous. No influence of the initial  
556 granular structure could be observed (Figure 5). This observation has also been made in other  
557 experimental works at laboratory scale (Hoffmann et al., 2007; Imbert and Villar, 2006; van Geet et  
558 al., 2005).

559 In the light of experimental results, considering two distinct domains in a conceptual approach is  
560 relevant, but attention must be drawn on the fact that distinction of two domains is a simplification of  
561 the material behaviour. Transition from the initial granular state to the final continuous state is likely  
562 to be more progressive. Nevertheless, the model was able to reproduce the evolution of swelling  
563 pressure in three swelling pressure tests performed on three different mixtures, using a single set of  
564 parameters.

565

#### 566 6.1.2. Transition criteria

567 The transition criteria have to determine conditions in which the material behaviour can no longer  
568 be considered controlled by the pellet assembly. Two criteria have been proposed: (i) The relative  
569 volume fraction of powder and pellets granular assemblies; (ii) suction at which the microstructure of  
570 bentonite rearrange, inducing changes of the macroscopic response under hydromechanical loadings.

571 For binary granular mixtures, the conceptual approach of the dominant phase (de Larrard, 2014;  
572 Roquier, 2015; Roux et al., 2007; Ueda et al., 2011; Westman and Hugill, 1930; Yerazunis et al.,  
573 1965) can estimate the volumetric proportion of fine particles corresponding to a transition between a  
574 macroscopic behaviour controlled by the assembly of coarse grains to a macroscopic behaviour  
575 controlled by the assembly of fine particles. However, in bentonite pellet and powder mixtures, pellets  
576 and powder grains swell, their volumetric strains are comparable, and the observed transition can  
577 occur at relative volumetric proportions close to the initial state. It is the reason why the  $r_{vf}$  parameter  
578 is introduced. Since pellets swell upon hydration, the available volume for powder grains to swell

579 decreases and the powder phase becomes progressively denser, even if the volumetric proportions are  
580 the same as the initial state. However, the determination of the threshold value  $r_{vf}^*$  is tricky. In the  
581 present work, a value of  $r_{vf}^* = 1$  was assumed. Since data was lacking, it was assumed that the pellet  
582 assembly can no longer control the macroscopic behaviour if the density of the powder grains in the  
583 inter-pellet porosity reaches the density of the pellet assembly. This choice is considered relevant by  
584 comparison with experiment. It was highlighted in the 70/30 test that the influence of powder was  
585 non-negligible for suction below 60 MPa. Using equations (30) and (31) assuming that  $p$  is negligible  
586 compared to  $s$  yields  $r_{vf}(s = 60 \text{ MPa}) = 1.05$ . However, it is likely that a single value of this parameter  
587 would not suit all mixtures. The  $r_{vf}^*$  parameter should be determined with care and not necessarily  
588 taken equal to 1.

589 In bentonite materials, experimental results (Saiyouri et al., 2004) evidence that exfoliation of clay  
590 particles occurs upon adsorption of water molecule layers. When the clay particle is no longer stable, a  
591 sharp decrease of the number of layers per particle is observed. For MX80 bentonite, this threshold is  
592 in the range 3-7 MPa and corresponds to the development of diffuse layers, microstructural  
593 rearrangements, modification of the pore size distribution, and change in the water retention behaviour  
594 (Keller et al., 2014; Molinero-Guerra et al., 2020; Saiyouri et al., 2004; Villar, 2007). MX80 pellets  
595 and powder (crushed pellets) are thus affected by significant microstructural rearrangement in this  
596 suction range. It is considered that the initial granular structure is not the main feature controlling the  
597 macroscopic response for suction below a threshold suction,  $s^*$ .

598

### 599 6.1.3. Granular material

600 The constitutive equations for the granular domain are based on DEM simulation results of large  
601 pellet assemblies. The use of DEM to simulate pellet assemblies from the behaviour of one pellet has  
602 been discussed in (Darde et al., 2020a). It was highlighted that modelling pellets by spheres of same  
603 diameter, same stiffness and same strength could induce an overestimation of the macroscopic  
604 stiffness of the mixture and of the peak pressure attributed to pellet strength, respectively related to  $f_{e a}$

605 and  $m_g^*$  in the present work. It was also evidenced that wall effects in small samples can influence the  
606 material behaviour.

607 In the present work, a value of  $f_{\varepsilon a} = 6$  was suggested from DEM results, which can also make the  
608 mixture stiffer in FEM simulation than in experiments (Figure 13a). The peak pressure in FEM  
609 simulations was also higher than in experiments. Nevertheless, both the macroscopic stiffness and  
610 peak pressure appeared to be in the right order of magnitude for all mixtures.

611 The post peak behaviour in the granular domain exhibits a moderate decrease followed by a  
612 moderate increase of swelling pressure. After the peak, the material macroscopic stiffness is mainly  
613 related to  $f_{\varepsilon b}$ . It is worthy to mention that in DEM, for  $m_g > m_g^*$ ,  $d\varepsilon_v/dm_g$  was increasing even if the  $\varepsilon_v$ -  
614  $m_g$  relationship appears sublinear (Figure 7). Thus, even if  $f_{\varepsilon b} = 40$  was suggested (from linear fit),  
615 higher values could have also been relevant.

616 It was demonstrated that  $\frac{\partial \varepsilon_v^{(e)}}{\partial \varepsilon_{V1}} = 1$  in a granular assembly with elastic contacts. This value has been  
617 used in all simulations. For plastic contacts,  $f_{Mm}$  progressively becomes smaller than 1. The assumption  
618 of a constant “elastic”  $f_{Mm}$  induces larger volumetric strain of the mixture upon pellet volume  
619 variations. However, as the macroscopic volumetric strain also depends on  $f_{\varepsilon b}$  through variations of  
620  $m_g$ , a convenient way of handling this problem is to choose a relevant couple ( $f_{Mm}, f_{\varepsilon b}$ ) to reproduce the  
621 behaviour of the mixture when  $m_g > m_g^*$ .

622 Finally, as presented in Figure 7, the repeatability of the results is very good. Variability associated  
623 to small size of the sample discussed in (Darde et al., 2020a) is avoided in the present study. The 4000  
624 particles periodic sample can be considered representative of a pellet assembly which allows the  
625 intrinsic behaviour of pellet assemblies to be addressed with few simulations.

626

#### 627 6.1.4. Continuous material

628 In the continuous domain, a modified BBM (Alonso et al., 1990) was proposed to model the  
629 material behaviour. This approach was also adopted to model bentonite-based pellet materials in other

630 studies by various authors (Alonso et al., 2011; Gens et al., 2011; Hoffmann et al., 2007; Mokni et al.,  
631 2020; Sánchez et al., 2016), with different modifications of the original modelling framework. In the  
632 present work, the BBM approach is used only for the continuous domain because it is not able to  
633 reproduce features observed in the laboratory such as the free swelling powder in the 70/15 mixture,  
634 the influence of the powder phase in the 70/30 mixture, or the two peaks of swelling pressure observed  
635 in the 70/0 mixture.

636 Compared to other numerical studies from the literature, the proposed modified BBM is simpler  
637 and does not account for features such as plasticity in the microstructure (Alonso et al., 2011) or  
638 damage in the microstructure (Mokni et al., 2020), partial saturation of the microstructure (Alonso et  
639 al., 2011; Sánchez et al., 2016), inter-aggregate porosity in the pellets (Navarro et al., 2020a, 2020b),  
640 or plastic macroscopic strain resulting from microstructural swelling (Gens et al., 2011; Mokni et al.,  
641 2020; Sánchez et al., 2016). Nevertheless, it is able to satisfactorily reproduce the evolution of  
642 swelling pressure for all mixtures, notably the 70/30 which was considered continuous in the  
643 simulation during most of the hydration path.

644 The simple model for the continuous domain must be regarded as part of the global approach,  
645 considering two domains. Even if it is simplified compared to traditional BBM-based modelling  
646 approaches, it aims at reproducing only the final part of the hydration path. It allows intrinsic features  
647 of the material behaviour to be directly accounted for, for instance change in the macroscopic response  
648 depending on the density of the powder phase, evolution of the macroscopic swelling potential with  
649 density, homogenisation of the mixture, using a single set of parameters.

650

#### 651 6.1.5. Hydraulic equilibrium

652 Hydraulic equilibrium was assumed during all the simulations for simplicity. In the case of pellet-  
653 powder mixture, owing to the low permeability and size difference between pellets and powder grains,  
654 it is likely that equation (20) is not realistic. (Gens et al., 2011) and (Sánchez et al., 2016) considered

655 two different suctions for pellets and powder in simulations with a simplified transfer law between the  
656 two levels of structure.

657 A consequence of the hydraulic equilibrium assumption is that pellet swelling would be too fast in  
658 simulations of hydration paths not performed at equilibrium as in the present experimental study (use  
659 of the vapour equilibrium technique).

660

## 661 **6.2. Ability to reproduce the material behaviour**

662

### 663 6.2.1. Two peaks in no-powder samples

664 In FEM simulation of the 70/0 tests, a first peak occurs at a suction of ~70 MPa as a consequence  
665 of contact forces reaching pellet strength. Macroscopic yielding occurs at suction of ~7 MPa and a  
666 second peak is reached as a result. This latter was also observed in experiments but at lower suction.  
667 The overestimation of  $f_{Mm}$  for  $m_g > m_g^*$  allowed the swelling pressure to reach the LC yield locus in the  
668 simulation earlier than expected from experimental results. Yet, the second peak in FEM occurs at a  
669 swelling pressure comparable to the second peak in the experiment.

670

### 671 6.2.2. Influence of the powder phase in loose powder samples

672 In the granular domain, the material response is well reproduced by the model (Figure 13b).  
673 Transition to the continuous domain and subsequent increase of swelling pressure in the simulation are  
674 found to occur earlier than in experiment. In experiment, swelling pressure remains nearly constant  
675 until a suction of 4 MPa. It can be suggested that pellets swell too rapidly in FEM simulation, thus  $\phi_{mat}$   
676 increases faster in the simulation and the transition is computed at higher suction. This would mean  
677 that equilibrium in experiment was not perfectly reached after each suction step. Another suggestion to  
678 explain this difference between simulation and experiment is that  $r_{vf}^*$  is not a constant value and may  
679 be higher in 70/15 mixture than in 70/30 mixture. Even if the swelling pressure at  $s = 4$  MPa is

680 overestimated, it is interesting to note that the overall response provided by the model is quite close to  
681 the experimental one, involving a succession of very different phenomena.

682

### 683 6.2.3. Swelling pressure evolution

684 In spite of some differences between simulations and experiments, Figure 13d highlights that the  
685 overall ability of the model to reproduce the evolution of swelling pressure is good. It predicts the  
686 significant influence of the initial granular structure in the 70/15 mixture and the moderate influence of  
687 the latter in the 70/30 mixture. It predicts also the trend of the evolution of swelling pressure rather  
688 well for all mixtures, either increase or plateau or decrease, at values of swelling pressure and suction  
689 close to experimental observation. Macroscopic yielding and peak phenomena are also well  
690 reproduced. The final swelling pressure is close to the experimental one in the three simulations.

691 In the model, irreversible strain can arise only if the transition criteria or the yield locus are  
692 reached. In experiments, only one hydration path has been performed. More complex hydration paths  
693 such as wetting-drying cycles, accumulating plastic strains, would not be properly reproduced by the  
694 present model.

695

### 696 6.2.4. Applicability to field conditions

697 In contact with liquid water, pellets would lose their granular structure (Hoffmann et al., 2007;  
698 Molinero-Guerra et al., 2019b) and the evolution of swelling pressure in the granular domain would  
699 not be observed. However, in field conditions, vapour diffusion is likely to be the dominant hydration  
700 mechanism (Kröhn, 2005). Thus, the influence of the initial granular structure is a relevant feature to  
701 take into account. Besides, local heterogeneities of density are likely to arise during installation in the  
702 galleries (Molinero-Guerra et al., 2017). Local heterogeneities of density influence the relative  
703 proportion of pellets and powder and the local value of the mixture dry density. Powder density has  
704 been shown to have a significant influence on the mechanical behaviour. In this regard, the proposed

705 model is relevant because it allows to account for heterogeneities of density with a single set of  
706 parameters. In repository conditions, hydration of the mixture will be progressive. Thus, the  
707 consideration of two different suctions for pellets and powder grains in the model would be necessary.

708

## 709 **7. Conclusion**

710 Bentonite pellet-powder mixtures are candidate materials for the sealing of galleries in radioactive  
711 waste disposal concepts. The mechanical behaviour of these materials is influenced by their initial  
712 granular structure and the density of the powder phase.

713 In the present study, swelling pressure tests have been carried out on three mixtures with the same  
714 pellet volume fraction and different powder contents. It was highlighted that the initial granular  
715 structure has no significant influence on the behaviour of mixtures with dense powder phase.  
716 Conversely, the powder phase has no significant influence on the behaviour of mixtures with loose  
717 powder phase until a low suction.

718 The behaviour of pellet assemblies has been studied under isotropic compression through DEM  
719 simulations. It was highlighted that the initial pellet volume fraction, pellet stiffness and pellet strength  
720 have a notable influence on the macroscopic behaviour of the pellet assembly. In addition, it was  
721 demonstrated that, upon pellet swelling, the volumetric strain of a pellet assembly is equal to the  
722 volumetric strain of the pellet under the assumption of elastic contact reaction.

723 Based on experimental and DEM results, a conceptual model for pellet-powder mixture has been  
724 proposed. The model is formulated in the framework of hardening elastoplasticity and considers two  
725 distinct domains in elasticity. Depending on suction and the density of the powder phase, the mixture  
726 is either considered granular or continuous. In the granular domain, the pellet assembly controls the  
727 behaviour of the mixture and constitutive laws are proposed from DEM results. In the continuous  
728 domain, pellets and powder contributes to the mechanical behaviour of the mixture and a modified  
729 BBM is used to model its behaviour.

730 The model was used to simulate the swelling pressure tests performed in the laboratory. Owing to  
731 its conceptual nature, some differences have been noted between numerical and experimental results.  
732 However, the numerical results generally reproduced very well the experimental results, using a single  
733 set of parameters for all mixtures. Swelling pressures obtained in simulations were very close to  
734 experimental ones. These results improve the knowledge on the behaviour of bentonite pellet-powder  
735 mixtures during hydration in constant-volume conditions.

736 An interesting perspective arising from the present work is a better characterisation of the transition  
737 from the behaviour controlled by the pellet assembly to the continuous behaviour, which is a  
738 progressive phenomenon. The influence of the powder density on the macroscopic response can be  
739 investigated in this respect. Besides, water transfer laws in pellets should be proposed to avoid the  
740 hypothesis of hydraulic equilibrium. The proposed modelling approach can then be used to provide  
741 interesting predictive simulations of pellet-powder mixtures in repository conditions, to better assess  
742 the long-term safety of these facilities.

743

#### 744 **Declaration of competing interests**

745 The authors declare that they have no known competing financial interests or personal relationships  
746 that could have appeared to influence the work reported in this paper.

747

#### 748 **List of references**

749 Agnolin, I., Roux, J.N., 2007. Internal states of model isotropic granular packings. I. Assembling  
750 process, geometry, and contact networks. *Phys. Rev. E - Stat. Nonlinear, Soft Matter Phys.* 76,  
751 1–27. <https://doi.org/10.1103/PhysRevE.76.061302>

752 Alonso, E.E., Gens, A., Josa, A., 1990. A constitutive model for partially saturated soils G ”.  
753 *Géotechnique* 40, 405–430. <https://doi.org/10.1680/geot.1990.40.3.405>

754 Alonso, E.E., Hoffmann, C., Romero, E., 2010. Pellet mixtures in isolation barriers. *J. Rock Mech.*

755 Geotech. Eng. 2, 12–31. <https://doi.org/10.3724/SP.J.1235.2010.00012>

756 Alonso, E.E., Romero, E., Hoffmann, C., 2011. Hydromechanical behaviour of compacted granular  
757 expansive mixtures: experimental and constitutive study. *Géotechnique* 61, 329–344.  
758 <https://doi.org/10.1680/geot.2011.61.4.329>

759 Bernachy-barbe, F., Conil, N., Guillot, W., Talandier, J., 2020. Observed heterogeneities after  
760 hydration of MX-80 bentonite under pellet/powder form. *Appl. Clay Sci.* 189, 105542.  
761 <https://doi.org/10.1016/j.clay.2020.105542>

762 Bian, X., Cui, Y., Li, X., 2019. Voids effect on the swelling behaviour of compacted bentonite.  
763 *Géotechnique* 69, 593–605. <https://doi.org/10.1680/jgeot.17.P.283>

764 Christoffersen, J., Mehrabadi, M.M., 1981. A Micromechanical Description of Granular Material  
765 Behavior. *J. Appl. Mech.* 48, 339–344.

766 Dangla, P., 2018. Bil-2.6 A modeling platform based on finite volume/element methods (Version  
767 v2.6). <https://doi.org/http://doi.org/10.5281/zenodo.1419841>

768 Darde, B., Roux, J.-N., Pereira, J.-M., Dangla, P., Talandier, J., Vu, M.N., Tang, A.M., 2020a.  
769 Investigating the hydromechanical behaviour of bentonite pellets by swelling pressure tests and  
770 discrete element modelling. *Acta Geotech.* <https://doi.org/10.1007/s11440-020-01040-5>

771 Darde, B., Tang, A.M., Pereira, J.-M., Roux, J.-N., Dangla, P., Talandier, J., Vu, M.N., 2018. Hydro-  
772 mechanical behaviour of high-density bentonite pellet on partial hydration. *Géotechnique Lett.* 8,  
773 330–335. <https://doi.org/10.1680/jgele.18.00114>

774 Darde, B., Tang, A.M., Roux, J., Dangla, P., Pereira, J., Talandier, J., Vu, M.N., 2020b. Effects of the  
775 initial granular structure of clay sealing materials on their swelling properties: experiments and  
776 DEM simulations. *Eur. Phys. J. Nucl. Sci. Technol.* 6.  
777 <https://doi.org/https://doi.org/10.1051/epjn/2019059>

778 de Larrard, F., 2014. Concrete mixture proportioning: a scientific approach. CRC Press.

779 Ferrari, A., Favero, V., Marschall, P., Laloui, L., 2014. Experimental analysis of the water retention

780 behaviour of shales. *Int. J. Rock Mech. Min. Sci.* 72, 61–70.  
781 <https://doi.org/10.1016/j.ijrmms.2014.08.011>

782 Gens, A., Valleján, B., Sánchez, M., Imbert, C., Villar, M.V., Van Geet, M., 2011. Hydromechanical  
783 behaviour of a heterogeneous compacted soil: experimental observations and modelling.  
784 *Géotechnique* 61, 367–386. <https://doi.org/10.1680/geot.SIP11.P.015>

785 Hoffmann, C., Alonso, E.E., Romero, E., 2007. Hydro-mechanical behaviour of bentonite pellet  
786 mixtures. *Phys. Chem. Earth* 32, 832–849. <https://doi.org/10.1016/j.pce.2006.04.037>

787 Imbert, C., Villar, M.V., 2006. Hydro-mechanical response of a bentonite pellets/powder mixture upon  
788 infiltration. *Appl. Clay Sci.* 32, 197–209. <https://doi.org/10.1016/j.clay.2006.01.005>

789 Jia, L., Chen, Y., Ye, W., Cui, Y., 2019. Effects of a simulated gap on anisotropic swelling pressure of  
790 compacted GMZ bentonite. *Eng. Geol.* 248, 155–163.  
791 <https://doi.org/10.1016/j.enggeo.2018.11.018>

792 Johnson, K.L., 1985. *Contact Mechanics*. Cambridge University Press, Cambridge, UK.  
793 <https://doi.org/10.1115/1.3261297>

794 Kaufhold, S., Baille, W., Schanz, T., Dohrmann, R., 2015. About differences of swelling pressure -  
795 dry density relations of compacted bentonites. *Appl. Clay Sci.* 107, 52–61.  
796 <https://doi.org/10.1016/j.clay.2015.02.002>

797 Keller, L.M., Seiphoori, A., Gasser, P., Lucas, F., Holzer, L., Ferrari, A., 2014. The pore structure of  
798 compacted and partly saturated MX-80 bentonite at different dry densities. *Clays Clay Miner.* 62,  
799 174–187. <https://doi.org/10.1346/CCMN.2014.0620302>

800 Kröhn, K.P., 2005. New evidence for the dominance of vapour diffusion during the re-saturation of  
801 compacted bentonite. *Eng. Geol.* 82, 127–132. <https://doi.org/10.1016/j.enggeo.2005.09.015>

802 Lloret, A., Villar, M. V, Sanchez, M., Gens, A., Pintado, X., Alonso, E., 2003. Mechanical behaviour  
803 of heavily compacted bentonite under high suction changes. *Geotechnique* 53, 27–40.  
804 <https://doi.org/10.1680/geot.53.1.27.37258>

805 Marcial, D., 2003. Comportement hydromécanique et microstructural des matériaux de barrière  
806 ouvragée. Doctoral dissertation, Ecole nationale des ponts et chaussées, France.

807 Mokni, N., Molinero-Guerra, A., Cui, Y.-J., Delage, P., Aïmedieu, P., Bornert, M., Tang, A.M., 2020.  
808 Modelling the long-term hydro-mechanical behaviour of a bentonite pellet/powder mixture with  
809 consideration of initial structural heterogeneities. *Géotechnique* 70, 563–580.  
810 <https://doi.org/10.1680/jgeot.18.p.110>

811 Molinero-Guerra, A., Cui, Y.J., He, Y., Delage, P., Mokni, N., Tang, A.M., Aïmedieu, P., Bornert, M.,  
812 Bernier, F., 2019a. Characterization of water retention, compressibility and swelling properties of  
813 a pellet/powder bentonite mixture. *Eng. Geol.* 248, 14–21.  
814 <https://doi.org/10.1016/j.enggeo.2018.11.005>

815 Molinero-Guerra, A., Delage, P., Cui, Y.-J., Mokni, N., Tang, A.M., Aïmedieu, P., Bernier, F.,  
816 Bornert, M., 2020. Water retention properties and microstructure changes of a bentonite pellet  
817 upon wetting/drying; application to radioactive waste disposal. *Géotechnique* 70, 199–209.  
818 <https://doi.org/10.1680/jgeot.17.p.291>

819 Molinero-Guerra, A., Mokni, N., Cui, Y., Delage, P., Tang, A.M., Aïmedieu, P., Bornert, M., 2019b.  
820 Impact of initial structural heterogeneity on long term swelling behavior of MX80 bentonite  
821 pellet/powder mixtures. *Can. Geotech. J.* <https://doi.org/10.1139/cgj-2018-0301>

822 Molinero-Guerra, A., Mokni, N., Delage, P., Cui, Y.J., Tang, A.M., Aïmedieu, P., Bernier, F., Bornert,  
823 M., 2017. In-depth characterisation of a mixture composed of powder/pellets MX80 bentonite.  
824 *Appl. Clay Sci.* 135, 538–546. <https://doi.org/10.1016/j.clay.2016.10.030>

825 Navarro, V., Asensio, L., Gharbieh, H., De, G., Pulkkanen, V., 2020a. A triple porosity hydro-  
826 mechanical model for MX-80 bentonite pellet mixtures. *Eng. Geol.* 265.  
827 <https://doi.org/10.1016/j.enggeo.2019.105311>

828 Navarro, V., Asensio, L., Morena, G. De, Gharbieh, H., Alonso, J., 2020b. From double to triple  
829 porosity modelling of bentonite pellet mixtures. *Eng. Geol.* 274.

- 830 <https://doi.org/10.1016/j.enggeo.2020.105714>
- 831 Roquier, G., 2015. Etude théorique des effets de paroi et de desserrement dans les mélanges  
832 granulaires. Doctoral dissertation, Ecole nationale des ponts et chaussées, France.
- 833 Roux, J.-N., Chevoir, F., Toussaint, F., 2007. Etats de compacité maximale pour les mélanges binaires  
834 de grains sphériques : étude par simulation numérique. Bull. des Lab. des Ponts Chaussées 268–  
835 269, 141–152.
- 836 Saba, S., Cui, Y., Tang, A.M., Barnichon, J., 2014. Investigation of the swelling behaviour of  
837 compacted bentonite-sand mixtures by mock-up tests. Can. Geotech. J. 51, 1399–1412.
- 838 Saiyouri, N., Hicher, P.Y., Tessier, D., 2000. Microstructural approach and transfer water modelling in  
839 highly compacted unsaturated swelling clays. Mech. Cohesive-frictional Mater. 5, 41–60.
- 840 Saiyouri, N., Tessier, D., Hicher, P.Y., 2004. Experimental study of swelling in unsaturated compacted  
841 clays. Clay Miner. 39, 469–479. <https://doi.org/10.1180/0009855043940148>
- 842 Sánchez, M., Gens, A., Villar, M.V., Olivella, S., 2016. Fully Coupled Thermo-Hydro-Mechanical  
843 Double-Porosity Formulation for Unsaturated Soils. Int. J. Geomech. D4016015.  
844 [https://doi.org/10.1061/\(ASCE\)GM.1943-5622.0000728](https://doi.org/10.1061/(ASCE)GM.1943-5622.0000728)
- 845 Tang, A.-M., Cui, Y.-J., 2005. Controlling suction by the vapour equilibrium technique at different  
846 temperatures and its application in determining the water retention properties of MX80 clay.  
847 Can. Geotech. J. 42, 287–296. <https://doi.org/10.1139/t04-082>
- 848 Ueda, T., Matsushima, T., Yamada, Y., 2011. Effect of particle size ratio and volume fraction on shear  
849 strength of binary granular mixture. Granul. Matter 13, 731–742. [https://doi.org/10.1007/s10035-](https://doi.org/10.1007/s10035-011-0292-1)  
850 [011-0292-1](https://doi.org/10.1007/s10035-011-0292-1)
- 851 van Geet, M., Volckaert, G., Roels, S., 2005. The use of microfocus X-ray computed tomography in  
852 characterising the hydration of a clay pellet/powder mixture. Appl. Clay Sci. 29, 73–87.  
853 <https://doi.org/10.1016/j.clay.2004.12.007>
- 854 Villar, M.V., 2005. MX80 bentonite. Thermo-Hydro-Mechanical Characterisation Performed at

- 855 CIEMAT in the Context of the Prototype Project. Inf. Técnicos Ciemat 1053.
- 856 Villar, M. V., 2007. Water retention of two natural compacted bentonites. *Clays Clay Miner.* 55, 311–  
857 322. <https://doi.org/10.1346/CCMN.2007.0550307>
- 858 Wang, Q., Tang, A.M., Cui, Y.J., Delage, P., Barnichon, J.D., Ye, W.M., 2013. The effects of  
859 technological voids on the hydro-mechanical behaviour of compacted bentonite-sand mixture.  
860 *Soils Found.* 53, 232–245. <https://doi.org/10.1016/j.sandf.2013.02.004>
- 861 Wang, Q., Tang, A.M., Cui, Y.J., Delage, P., Gatmiri, B., 2012. Experimental study on the swelling  
862 behaviour of bentonite/claystone mixture. *Eng. Geol.* 124, 59–66.  
863 <https://doi.org/10.1016/j.enggeo.2011.10.003>
- 864 Westman, A.E.R., Hugill, H.R., 1930. the Packing of Particles. *J. Am. Ceram. Soc.* 13, 767–779.  
865 <https://doi.org/10.1111/j.1151-2916.1930.tb16222.x>
- 866 Yerazunis, S., Cornel, S.W., Wintner, B., 1965. Dense random packing of binary mixtures of spheres.  
867 *Nature* 207, 835.
- 868 Zhang, Z., Ye, W., Liu, Z., Wang, Q., Cui, Y., 2020. Mechanical behavior of GMZ bentonite pellet  
869 mixtures over a wide suction range. *Eng. Geol.* 264, 105383.  
870 <https://doi.org/10.1016/j.enggeo.2019.105383>

871

## 872 **Appendix A**

873 In a granular assembly, the diagonal components of the Cauchy stress tensor can be written as  
874 follows:

$$\sigma_{\alpha\alpha} = \frac{1}{\Omega} \left( \sum_{i=1}^{N_c} F_{N\alpha} r_{\alpha} \right) \quad (52)$$

875 where  $\alpha$  is the reference coordinate axis ( $1 \leq \alpha \leq 3$ ),  $\Omega$  is the total volume of the granular assembly,  $N_c$   
876 is the number of contacts,  $r_{\alpha}$  are the  $\alpha$ -coordinates of vector  $\mathbf{r}$  joining the centre of particles in contact,

877  $F_{N\alpha}$  are the  $\alpha$ -coordinates of the corresponding contact force  $F_N$  (Agnolin and Roux, 2007;  
 878 Christoffersen and Mehrabadi, 1981). From this expression, the mean stress  $p$  in the granular assembly  
 879 is written as:

$$p = \frac{1}{3\Omega} \sum_{\alpha=1}^3 \left( \sum_{i=1}^{N_c} F_{N\alpha} r_{\alpha} \right) \quad (53)$$

880 The volume fraction of pellet  $\Phi_l$  and the coordination number  $Z$  of the granular assembly are  
 881 written as follows:

$$\Phi_1 = \frac{N_1 \Omega_1}{\Omega} \quad (54)$$

882 And

$$Z = \frac{2N_c}{N_1} \quad (55)$$

883 where  $N_l$  is the number of spheres and  $\Omega_l$  is the sphere volume.

884 From (54) and (55), in conditions where normal deflection at contact is negligible compared to the  
 885 sphere diameters (*i.e.*  $r_{\alpha} \approx a$ ), (53) can be written as:

$$p = \frac{Z\Phi_1}{\pi a^2} F_N^* \quad (56)$$

886 where  $F_N^*$  is the mean contact normal force in the granular assembly.

887 From equations (5) and (56), the following expression can be written:

$$\left(\frac{p}{\frac{E_1}{1-\nu_1^2}}\right)^{\frac{2}{3}} = \frac{\delta_N^*}{a} \left(\frac{Z \Phi_1}{3\pi}\right)^{\frac{2}{3}} \quad (57)$$

888 where  $\delta_N^*$  is the average normal deflection. From equation (57), the dimensionless parameter  $m_g$  is  
 889 defined as:

$$m_g = \left(\frac{p}{\frac{E_1}{1-\nu_1^2}}\right)^{\frac{2}{3}} \quad (58)$$

890

## 891 **Appendix B**

892 In a granular assembly of spherical particles, considering elastic contacts and particle volume  
 893 increase at constant particle stiffness and particle Young modulus, the mean stress in the granular  
 894 assembly can be written from the Hertz law (equation (5)) and equation (56):

$$p_0 = \frac{1}{3 \Omega_0} N_c \overline{(r_0 F_{N0})} \quad (59)$$

$$p = \frac{1}{3 \Omega_0 (1 + \varepsilon_V)} N_c \overline{\left(r_0 (1 + \varepsilon_V)^{\frac{1}{3}} F_N\right)} \quad (60)$$

895 Where  $p_0$  and  $F_{N0}$  are the values of  $p$  and  $F_N$  before particle swelling  $\Omega_0$  is the initial value of  $\Omega$ ,  $r_0$   
 896 is the initial value of  $r$ , the norm of the  $\mathbf{r}$  vector, and the horizontal bar denotes the average value over  
 897 all contacts.  $F_N$ , accounting for the volume variations of the granular assembly resulting from the  
 898 volume variations of the spherical particles, is written:

$$F_N = \frac{1}{3} E_1 (a_0)^{\frac{1}{2}} (1 + \varepsilon_{V1})^{\frac{1}{6}} \left[ r_0 (1 + \varepsilon_V)^{\frac{1}{3}} - a_0 (1 + \varepsilon_{V1})^{\frac{1}{3}} \right]^{\frac{3}{2}} \quad (61)$$

899       Where  $a_0$  is the initial value of  $a$ . In equations (60) and (61) ,  $r_0(1 + \varepsilon_V)^{\frac{1}{3}}$  and  $r_0(1 + \varepsilon_V)^{\frac{1}{3}} -$   
900  $a_0(1 + \varepsilon_{V1})^{\frac{1}{3}}$  respectively denotes the distance between two spherical particles in contacts and the  
901 deflection in contact between two spherical particles.

902       Following a small increase in the particle volumes, if no rearrangement of the granular assembly  
903 occurs and  $N_c$  remains constant, then

$$p = p_0 \leftrightarrow \varepsilon_V = \varepsilon_{V1} \quad (62)$$

904       Thus

$$f_{Mm} = \frac{\partial \varepsilon_V^{(e)}}{\partial \varepsilon_{V1}} = 1 \quad (63)$$

905

906

907 **List of Figures**

908 Figure 1: a) Picture of a pellet; b) Schematic view of a pellet.

909 Figure 2: Schematic view of the experimental setup. Red arrows represent humid air circulation.

910 Figure 3: Evolution of swelling pressure as a function of elapsed time. a) SP0a test, b) SP0b test, c)  
911 SP15 test, d) SP30 test.

912 Figure 4: Evolution of swelling pressure as a function of suction upon hydration. a) Swelling  
913 pressure on a logarithmic scale, b) Swelling pressure on a linear scale, limited to swelling pressures  
914 lower than 2 MPa. Horizontal arrows represent the final swelling pressure of the tested materials.

915 Figure 5: Pictures of SP0 samples. a) SP0a at 9 MPa of suction, b) SP0b following liquid water  
916 saturation. The cell diameter is 60 mm.

917 Figure 6: Conceptual interpretation of the behaviour of pellet-powder materials upon hydration in  
918 constant-volume conditions. The red solid lines represent the influence of the initial granular structure.  
919 The blue dashed lines represent the behaviour after the transition to the continuous domain.

920 Figure 8: Evolution of  $\varepsilon_V$  as a function of  $m_g$  during isotropic compression for all granular  
921 assemblies. a) A samples, b) B samples, c) C samples, d) D samples, e) E samples, f) comparison  
922 between A1, B1, C1, D1, E1.

923 Figure 9: Comparison of the evolution of  $x_{plas}$  as a function of  $m_g$  for the five types of granular  
924 assemblies.

925 Figure 10: Relationship between  $m_g^*$  and  $\Phi_{10}$  for all samples. The dashed line represents the fit  
926 corresponding to  $m_g^* = 0.067 \Phi_{10} - 0.031$ .

927 Figure 11: Preconsolidation pressure as a function of the void ratio in oedometer tests performed on  
928 bentonite materials by Molinero-Guerra et al. (2019) (Molinero-Guerra et al., 2019a), Villar (2005)  
929 (Villar, 2005), and Marcial (2003) (Marcial, 2003). The green dashed line is obtained using equation  
930 (59) with  $p_r = 80$  MPa and  $n_p = 3.7$ .

931 Figure 12: Sketch of the model elastic domain: a) in the  $p$ - $s$  plane, b) partition of the elastic domain  
932 in the granular and continuous domains.

933 Figure 13: Geometry of the FEM simulations. Lengths are given in m.

934 Figure 14: Comparison between FEM simulation and experimental results of swelling pressure  
935 tests for a) 70/0 material; b) 70/15 material; c) 70/30 material, d) comparison of all FEM simulation  
936 and experimental results.

937

938 **List of Tables**

939 Table 1: Initial properties of the pellets.

940 Table 2: Properties of the pellet-powder mixtures.

941 Table 3: Hydration paths followed by the samples. Suctions are given in MPa.

942 Table 4: Parameters of the model for a pellet.

943 Table 5: Initial properties of the numerical samples. All samples are cubic and contain 4000  
944 spheres.

945 Table 6: Summary of the model equations related to the volumetric strains.

946 Table 7: Model parameters related to the mixture properties.

947 Table 8: Model parameters related to the elastic behaviour of the material.

948 Table 9: Model parameters related to the granular-continuous transition.

949 Table 10: Model parameters related to the plastic behaviour of the material.

950